

# The Hydrangea simulations: galaxy formation in and around massive clusters

Yannick M. Bahé,<sup>1★</sup> David J. Barnes,<sup>2</sup> Claudio Dalla Vecchia,<sup>3,4</sup> Scott T. Kay,<sup>2</sup> Simon D. M. White,<sup>1</sup> Ian G. McCarthy,<sup>5</sup> Joop Schaye,<sup>6</sup> Richard G. Bower,<sup>7</sup> Robert A. Crain,<sup>5</sup> Tom Theuns,<sup>7</sup> Adrian Jenkins,<sup>7</sup> Sean L. McGee,<sup>8</sup> Matthieu Schaller,<sup>7</sup> Peter A. Thomas<sup>9</sup> and James W. Trayford<sup>7</sup>

<sup>1</sup>Max-Planck-Institut für Astrophysik, Karl-Schwarzschild Str. 1, D-85748 Garching, Germany

<sup>2</sup>Jodrell Bank Centre for Astrophysics, School of Physics and Astronomy, The University of Manchester, Manchester M13 9PL, UK

<sup>3</sup>Instituto de Astrofísica de Canarias, C/Vía Láctea s/n, E-38205 La Laguna, Tenerife, Spain

<sup>4</sup>Departamento de Astrofísica, Universidad de La Laguna, Av. del Astrofísico Francisco Sánchez s/n, E-38206 La Laguna, Tenerife, Spain

<sup>5</sup>Astrophysics Research Institute, Liverpool John Moores University, 146 Brownlow Hill, Liverpool L3 5RF, UK

<sup>6</sup>Leiden Observatory, Leiden University, P.O. Box 9513, NL-2300 RA Leiden, the Netherlands

<sup>7</sup>Institute for Computational Cosmology, Department of Physics, University of Durham, South Road, Durham DH1 3LE, UK

<sup>8</sup>School of Physics and Astronomy, University of Birmingham, Edgbaston, Birmingham B15 2TT, UK

<sup>9</sup>Astronomy Centre, University of Sussex, Falmer, Brighton BN1 9QH, UK

Accepted 2017 June 5. Received 2017 May 31; in original form 2017 March 8

## ABSTRACT

We introduce the Hydrangea simulations, a suite of 24 cosmological hydrodynamic zoom-in simulations of massive galaxy clusters ( $M_{200c} = 10^{14}–10^{15.4} M_{\odot}$ ) with baryon particle masses of  $\sim 10^6 M_{\odot}$ . Designed to study the impact of the cluster environment on galaxy formation, they are a key part of the ‘Cluster–EAGLE’ project. They use a galaxy formation model developed for the EAGLE project, which has been shown to yield both realistic field galaxies and hot gas fractions of galaxy groups consistent with observations. The total stellar mass content of the simulated clusters agrees with observations, but central cluster galaxies are too massive, by up to 0.6 dex. Passive satellite fractions are higher than in the field, and at stellar masses  $M_{\text{star}} > 10^{10} M_{\odot}$ , this environmental effect is quantitatively consistent with observations. The predicted satellite stellar mass function matches data from local cluster surveys. Normalized to total mass, there are fewer low-mass ( $M_{\text{star}} \lesssim 10^{10} M_{\odot}$ ) galaxies within the virial radius of clusters than in the field, primarily due to star formation quenching. Conversely, the simulations predict an overabundance of massive galaxies in clusters compared to the field that persists to their far outskirts ( $> 5 r_{200c}$ ). This is caused by a significantly increased stellar mass fraction of (sub-)haloes in the cluster environment, by up to  $\sim 0.3$  dex even well beyond  $r_{200c}$ . Haloes near clusters are also more concentrated than equally massive field haloes, but these two effects are largely uncorrelated.

**Key words:** methods: numerical – galaxies: clusters: general – galaxies: stellar content.

## 1 INTRODUCTION

In the local Universe, strong correlations exist between the properties of galaxies and their large-scale environment. In particular, galaxies in groups and clusters are typically red, lack recent and ongoing star formation (e.g. Balogh et al. 1999; Kauffmann et al. 2004; Weinmann et al. 2006; Peng et al. 2010; Wetzel, Tinker & Conroy 2012), are depleted in atomic hydrogen (HI; Giovanelli &

Haynes 1985; Fabello et al. 2012; Hess & Wilcots 2013), and biased towards early-type (elliptical) morphologies (e.g. Dressler 1980).

However, all of these properties are also observed to correlate with galaxy luminosity and stellar mass, so that it is possible that these differences stem, at least in part, from different stellar mass distributions between dense environments and the field. The luminosity function of cluster galaxies has been studied by several authors in the last decade (e.g. Popesso et al. 2006; Agulli et al. 2014, 2016; Lan, Ménard & Mo 2016). Some of these works indeed found significant variations of the luminosity function between clusters and the field, especially in the form of a steep faint-end upturn

★ E-mail: ybahe@mpa-garching.mpg.de

in clusters (Popesso et al. 2006; Lan et al. 2016). However, the deep observations of the cluster Abell 85 by Agulli et al. (2014, 2016) found no evidence for such a steep upturn. This uncertainty complicates the interpretation of the observed environmental variations of galaxy properties.

Stellar mass is arguably a more fundamental quantity than luminosity, but its determination requires estimating the mass-to-light ratio from galaxy colours (e.g. Bell & de Jong 2001), or, if available, spectra (e.g. Kauffmann et al. 2003a; Gallazzi et al. 2005). From an analysis of Sloan Digital Sky Survey (SDSS) spectroscopic data, Kauffmann et al. (2004) demonstrated that a larger fraction of stellar mass in dense environments is contributed by more massive galaxies compared to low-density regions. Subsequent studies have suggested that this shift is driven mainly by the special properties of central cluster galaxies (e.g. von der Linden et al. 2010; Calvi et al. 2013), for example report that the shape of the *satellite* stellar mass function in clusters is similar to that in the field, at least at the massive end. Several other authors, however, have found differences between the satellite and field stellar mass functions, at either the high- or low-mass end (Yang et al. 2009; Wang & White 2012; Vulcani et al. 2014). In part, these differences may be driven by different definitions of ‘environment’ (local density, halo mass, and radial range) and differences in accounting for fore-/background galaxies.

An observational consensus on the nature of stellar mass differences in different environments would clearly be desirable, but even in its absence one can gain valuable insight into the expected extent of, and physical reason underlying, such differences through predictions from theoretical galaxy formation models. Cosmological hydrodynamic simulations are able to self-consistently predict differences in the formation of central and satellite galaxies, without explicitly prescribing the action of specific processes affecting only the latter. This gives them, in principle, great predictive power to understand the star formation histories of cluster galaxies as manifested in their present-day stellar masses.

However, such simulations have for a long time been unable to predict a galaxy stellar mass function (GSMF) in the field that agrees with observations (e.g. Crain et al. 2009; Scannapieco et al. 2012), which is clearly a pre-requisite for making meaningful predictions about galaxies in clusters. This problem has been solved only recently, thanks to increased resolution and, in particular, significant efforts to improve and calibrate the subgrid models that the simulations employ to model the unresolved aspects of feedback from star formation and accreting supermassive black holes (BHs). With these improvements, the EAGLE (Schaye et al. 2015; Crain et al. 2015) project has produced a simulation that could be calibrated to match the observed stellar mass function and sizes of present-day field galaxies (see also Vogelsberger et al. 2014 and Dubois et al. 2014 for the similarly successful Illustris and Horizon-AGN projects). Apart from these calibrated matches, EAGLE has also successfully reproduced, amongst others, the observed colour bimodality of galaxies (Trayford et al. 2015), the evolution of galaxy sizes and star formation rates (SFRs, Furlong et al. 2015, 2017), their BH mass function (Rosas-Guevara et al. 2016) and the correlation between galactic star formation and BH accretion rates (McAlpine et al. 2017), their atomic (Rahmati et al. 2015; Bahé et al. 2016; Crain et al. 2017) and molecular hydrogen content (Lagos et al. 2015), and the environmental effect of galaxy groups on atomic hydrogen (Marasco et al. 2016) and galaxy metallicity (Bahé et al. 2017).

Galaxy clusters, however, occupy only a small volume fraction of the Universe, so that simulation volumes much larger than available

in EAGLE are necessary to sample them in representative numbers. Such simulations can, at present, only afford a much lower resolution of  $\gtrsim 5$  kpc in spatial terms or particle masses of  $m_{\text{baryon}} \approx 10^9 M_{\odot}$  (e.g. Le Brun et al. 2014; Bocquet et al. 2016; McCarthy et al. 2017), compared to 0.7 kpc and  $\sim 10^6 M_{\odot}$  for EAGLE. This precludes studying even basic predictions such as stellar masses for galaxies with  $M_{\text{star}} \lesssim 10^{10} M_{\odot}$ , while more numerically sensitive properties such as their atomic gas content or metallicity are inaccessible for all but the most massive galaxies.

Until simulations at the resolution of EAGLE, but with orders-of-magnitude larger volume, become computationally feasible, progress can still be made through zoom-in simulations, where only a small, carefully selected volume inside a much larger parent simulation is modelled at high resolution and including baryons. The bulk of the volume is instead filled with low-resolution boundary particles interacting only through gravity, whose purpose is the creation of appropriate tidal fields and large-scale modes in the high-resolution region (e.g. Katz & White 1993; Tormen, Bouchet & White 1997; Borgani et al. 2002; Dolag et al. 2009; Ragone-Figueroa et al. 2013; Martizzi et al. 2014; Barnes et al. 2017a; Hahn et al. 2017).

Motivated by these considerations, this paper introduces the *Hydrangea* simulation project,<sup>1</sup> a suite of 24 high-resolution zoom-in galaxy clusters run with the EAGLE code for the purpose of studying the interaction between clusters and the galaxies in and around them. Each high-resolution simulation region is centred on a massive cluster ( $M_{200c} = 10^{14.0} - 10^{15.4} M_{\odot}$ ),<sup>2</sup> and realized at the same resolution level as the largest-volume simulation of the EAGLE project ( $m_{\text{baryon}} = 1.81 \times 10^6 M_{\odot}$ , gravitational softening length  $\epsilon = 0.7$  physical kpc at  $z < 2.8$ ). The high-resolution zoom-in region is set up to include not only the cluster haloes themselves, but also their large-scale surroundings out to 10 virial radii, i.e.  $\sim 10$ –25 comoving Mpc, motivated by indications from observations (e.g. von der Linden et al. 2010; Lu et al. 2012; Wetzel et al. 2012) and theory (Bahé et al. 2013) that the environmental influence on at least some galaxy properties extends significantly beyond the virial radius.

In this paper, we present a validation of the simulations in terms of some of the most fundamental galaxy properties, namely their stellar mass function and quenched fractions at  $z \approx 0$ , and then use the detailed information provided by the simulations to gain insight into the impact of the cluster environment on the GSMF. In a companion paper (Barnes et al. 2017b), we analyse the properties of the hot intracluster medium (ICM) in a sample of simulated clusters including the Hydrangea suite, and demonstrate that the simulations predict X-ray and Sunyaev-Zel’dovich (SZ) properties that are broadly compatible with low-redshift observational constraints. Predictions for the galaxy luminosity functions in our simulations, including results from a higher resolution run of an intermediate-mass cluster, will be presented by Dalla Vecchia et al. (in preparation). Together, these simulations form the ‘C-EAGLE’ project family.<sup>3</sup>

This paper is structured as follows. In Section 2, we review the EAGLE galaxy formation model that was used in our simulations, and describe the selection and simulation of the clusters that form

<sup>1</sup> Named after the plant *Hydrangea macrophylla*, whose petals change their colour from blue to red according to their environment, in analogy to the colour–density relation of galaxies.

<sup>2</sup>  $M_{200c}$  denotes the total mass within a sphere of radius  $r_{200c}$ , centred on the potential minimum of the cluster, within which the average density equals 200 times the critical density.

<sup>3</sup> ‘Cluster-EAGLE’, also referring to Steller’s sea eagle (*Haliaeetus pelagicus*) as the largest member of the avian eagle family.

the Hydrangea suite. We then compare several key predictions of the simulations to  $z \approx 0$  observations in Section 3, followed by a detailed analysis of the simulated stellar mass function in Section 4. Our results are then summarized and discussed in Section 5.

Throughout the paper, we adopt the same flat  $\Lambda$ CDM dark matter ( $\Lambda$ CDM) cosmology as used in the EAGLE simulations, with parameters as determined by Planck Collaboration XVI (2014b): Hubble parameter  $h \equiv H_0/(100 \text{ km s}^{-1} \text{ Mpc}^{-1}) = 0.6777$ , dark energy density parameter  $\Omega_\Lambda = 0.693$  (dark energy equation of state parameter  $w = -1$ ), matter density parameter  $\Omega_M = 0.307$ , and baryon density parameter  $\Omega_b = 0.04825$ . For length-scales, the prefix ‘p’ and ‘c’ denotes physical and comoving quantities, respectively (e.g. ‘pkpc’ for ‘physical kpc’); where no prefix is given, distances are given in physical units. Unless otherwise specified, all galaxy stellar masses are computed as the sum of gravitationally bound star particles within 30 pkpc from the potential minimum of their subhalo (see Schaye et al. 2015).

## 2 DESCRIPTION OF THE SIMULATIONS

In this section, we first provide a summary of the key features of the EAGLE code that was used for this work (Section 2.1), and then describe the setup and running of the Hydrangea cluster simulations (Section 2.2).

### 2.1 The EAGLE galaxy formation model

The simulation code developed for the EAGLE project is a substantially modified version of the GADGET-3 smoothed particle hydrodynamics (SPH) code, last described in Springel (2005). We restrict our description here to a summary of only its key features and refer the interested reader to the detailed description by Schaye et al. (2015).

Compared to GADGET-3, the hydrodynamics and time-stepping scheme has undergone several updates that are collectively referred to as ‘Anarchy’ (Dalla Vecchia, in preparation; see also appendix A of Schaye et al. 2015; Schaller et al. 2015c). These include using the conservative pressure-entropy formulation of SPH (Hopkins 2013), an artificial viscosity switch (Cullen & Dehnen 2010), an artificial conduction switch similar to that of Price (2008), the  $C^2$  Wendland (1995) kernel, and the time-step limiter proposed by Durier & Dalla Vecchia (2012). These updates mitigate many of the shortcomings of ‘traditional’ SPH codes, such as the treatment of surface discontinuities, described by e.g. Agertz et al. (2007) and Mitchell et al. (2009). Schaller et al. (2015c) discuss the impact of these modifications on the simulated galaxies in detail, and show that the most significant change is due to the Durier & Dalla Vecchia (2012) time-step limiter. These authors also demonstrated that the improved hydrodynamics implementation is a key requirement for the efficient action of feedback from supermassive BHs, as described further below.

Most importantly, the code contains subgrid physics models that were evolved from those developed for the OWLS (Schaye et al. 2010) simulation project.

Radiative cooling and photoheating rates are computed on an element-by-element basis following Wiersma, Schaye & Smith (2009a), by considering the 11 most important atomic coolants (H, He, C, N, O, Ne, Mg, Si, S, Ca, and Fe) in ionization equilibrium and in the presence of a Haardt & Madau (2001) ionizing UV/X-ray background. As discussed by Schaye et al. (2015), the code does not account for self-shielding of gas, because in the regime where this is expected to be important ( $n_H \gtrsim 10^{-2} \text{ cm}^{-3}$ ), the uncertain

effect of local stellar radiation would also need to be considered (Rahmati et al. 2013).

The modelling of reionization follows Wiersma et al. (2009b). To account for hydrogen reionization, the Haardt & Madau (2001) background is switched on at redshift  $z = 11.5$  (Theuns et al. 2002a; Planck Collaboration I 2014a). This is accompanied by the injection of 2 eV of energy per proton mass. He reionization is modelled by injecting the same amount of energy around  $z = 3.5$ , which results in a thermal evolution of the intergalactic medium (IGM) in agreement with the observations of Schaye et al. (2000, see also Theuns et al. 2002b).

The SFR of gas particles is modelled as a pressure law following Schaye & Dalla Vecchia (2008),

$$\dot{m}_{\text{star}} = m_g A (1 \text{ M}_\odot \text{ pc}^{-2})^{-n} \left( \frac{\gamma}{G} P \right)^{(n-1)/2}, \quad (1)$$

where  $\dot{m}_{\text{star}}$  is the SFR of a gas particle with mass  $m_g$  and (total) pressure  $P$ ,  $\gamma = 5/3$  is the ratio of specific heats, and  $G$  the gravitational constant. The subgrid parameters  $A = 1.515 \times 10^{-4} \text{ M}_\odot \text{ yr}^{-1} \text{ kpc}^{-2}$  and  $n = 1.4$  are then directly prescribed by observations (Kennicutt 1998), independent of any imposed equation of state. Deviating from Schaye & Dalla Vecchia (2008), the star formation threshold  $n_H^*$  depends on metallicity, as proposed by Schaye (2004):

$$n_H^*(Z) = 10^{-1} \text{ cm}^{-3} \left( \frac{Z}{0.002} \right)^{-0.64}, \quad (2)$$

where  $Z$  is the gas-phase metallicity smoothed over the SPH kernel (see Wiersma et al. 2009b). This equation accounts for the metallicity dependence of the transition from the warm atomic to the cold molecular interstellar gas phase.  $n_H^*(Z)$  is limited to a maximum of  $10 \text{ cm}^{-3}$  to prevent divergence at low  $Z$ . Star formation is then implemented stochastically with the probability of a gas particle being converted to a star set by equation (1). Because the simulations lack the resolution and physics to directly model the cold dense gas phase in which star formation is observed to occur in the real Universe, a pressure floor corresponding to  $P_{\text{eos}} \propto \rho_g^{4/3}$  is imposed on gas with  $n_H \geq 10^{-1} \text{ cm}^{-3}$ , normalized to  $T_{\text{eos}} = 8 \times 10^3 \text{ K}$  at that density. As this relation corresponds to a constant Jeans mass, it prevents artificial fragmentation due to a lack of numerical resolution (Schaye & Dalla Vecchia 2008).

Mass and metal enrichment of gas due to stellar mass loss is modelled as described by Wiersma et al. (2009b) with the modifications described in Schaye et al. (2015). This approach is based on treating star particles as simple stellar populations with a Chabrier (2003) initial mass function in the mass range  $0.1\text{--}100 \text{ M}_\odot$  and accounting for winds from asymptotic giant branch and massive stars as well as type-Ia and core-collapse supernovae.

Energy feedback from star formation is implemented in a single thermal mode, by heating a small number of gas particles ( $\sim 1$ ) by a large temperature increment ( $\Delta T = 10^{7.5} \text{ K}$ ). Dalla Vecchia & Schaye (2012) demonstrate that this approach alleviates numerical overcooling without the need to temporarily disable hydrodynamic forces or radiative cooling for affected gas particles, but can still not avoid it completely in the regions where the gas density is highest, and the cooling time therefore shortest. As discussed in detail by Crain et al. (2015), the efficiency of star formation feedback is therefore scaled with gas density so that energy input in dense regions formally exceeds the physically available energy budget from core-collapse supernovae. Averaged over the entire simulation, however, the ratio is below unity. In addition, the efficiency is lowered in high-metallicity gas to account for the physically expected higher cooling losses. Crain et al. (2015) show that these scalings of star formation

feedback efficiency are crucial for obtaining galaxies with realistic sizes, although the total galaxy masses are largely insensitive to them.

We note that, as an undesired side effect, these high-energy, stochastic, local heating events produce gas discs in some simulated galaxies that contain artificially large holes (Bahé et al. 2016). As we discuss further in Section 3.2, these holes may affect the predicted interaction between the dense cold gas discs and the hot intracluster gas in our simulations.

Finally, the code includes a model for the growth of supermassive BHs, which are seeded in a friends-of-friends (FoF) halo once its mass exceeds  $10^{10} h^{-1} M_{\odot}$  (Springel, Di Matteo & Hernquist 2005a) with a (subgrid) BH seed mass of  $10^5 h^{-1} M_{\odot}$ . Subsequently, the subgrid BH mass grows as a consequence of gas accretion, which is modelled as in Rosas-Guevara et al. (2015) but without the Booth & Schaye (2009) ‘boost factor’ (Schaye et al. 2015). In essence, this approach considers the angular momentum of gas near the BH to limit the Bondi accretion rate to

$$\dot{m}_{\text{accr}} = \dot{m}_{\text{Bondi}} \times \min \left( C_{\text{visc}}^{-1} (c_s/V_{\phi})^3, 1 \right) \quad (3)$$

where  $c_s$  is the sound speed and  $V_{\phi}$  the rotation speed of gas around the BH. The parameter  $C_{\text{visc}}$  was thought to set the stellar mass at which accretion becomes efficient (Rosas-Guevara et al. 2015). However, Bower et al. (2017) have shown that this scale is instead determined by the critical halo mass above which the hot hydrostatic atmosphere traps outflows driven by star formation and is nearly independent of  $C_{\text{visc}}$ . In the EAGLE reference model (‘Ref’),  $C_{\text{visc}} = 2\pi$ .

In analogy to star formation, energy feedback from supermassive BHs (‘AGN feedback’) is implemented stochastically, with one particle heated by a large temperature increment. Following Booth & Schaye (2009), 15 per cent of the accreted rest mass is converted to energy, with a 10 per cent coupling efficiency to the surrounding gas, i.e. an energy injection rate of  $0.015 \dot{m}_{\text{accr}} c^2$  (where  $c$  is the speed of light). Because the gas surrounding supermassive BHs is typically denser than around newly formed stars, the temperature increment  $\Delta T_{\text{AGN}}$  must also be higher to make the feedback efficient. In the Ref model, one particle per heating event is heated by  $\Delta T_{\text{AGN}} = 10^{8.5}$  K. However, Schaye et al. (2015) have shown that this predicts X-ray luminosities and hot gas fractions in galaxy groups and intermediate-mass clusters that are higher than observed.

An alternative model that differs from Ref only in its choice of  $\Delta T_{\text{AGN}}$  ( $=10^9$  K) and  $C_{\text{visc}}$  ( $=2\pi \times 10^2$ ), ‘AGNdT9’, was shown to largely resolve these discrepancies on the scale of galaxy groups, while achieving a similarly good match as Ref to observed properties on galactic scales.<sup>4</sup> As discussed by Schaye et al. (2015), the increased heating temperature makes individual heating events more energetic and hence reduces numerical cooling losses. The increased value of  $C_{\text{visc}}$  was motivated by a better fit of the GSMF to observations. We therefore adopt the AGN feedback parametrization of AGNdT9 for all C-EAGLE simulations, including the Hydrangea suite presented here. In a companion paper (Barnes et al. 2017b), we show that this model also leads to simulated clusters with overall realistic ICM properties, albeit with a still somewhat too high hot gas mass fraction (by  $\sim 2\sigma$ ), and artificially high entropy levels in the cluster cores.

<sup>4</sup> Because AGNdT9 was only realized in a  $(50 \text{ cMpc})^3$  simulation volume, it contains only one halo whose mass at  $z = 0$  is (just) above  $10^{14} M_{\odot}$ . Schaye et al. (2015) could therefore not test its predictions on the hot gas properties in massive clusters.

## 2.2 The Hydrangea simulations

### 2.2.1 Selection of the C-EAGLE cluster sample

The reason for the absence of massive galaxy clusters in the original EAGLE simulations is their relatively small volume of  $\leq (100 \text{ cMpc})^3$ . Our new simulations are therefore based on a much larger ‘parent simulation’, described by Barnes et al. (2017a). This is a  $(3200 \text{ cMpc})^3$  volume which was simulated with dark matter only (DMO), in the same cosmology as that adopted for the EAGLE project (Planck Collaboration XVI 2014b, see Introduction). The DM particle mass in the parent simulation is  $8.01 \times 10^{10} M_{\odot}$  with a gravitational softening length of 59 kpc; a galaxy cluster with  $M > 10^{14} M_{\odot}$  is therefore resolved by at least 1000 particles.

From the parent simulation snapshot at  $z = 0$ , we then selected candidate clusters for zoom-in re-simulation. Apart from a threshold in halo mass ( $M_{200c} \geq 10^{14} M_{\odot}$ ), we also applied a mild isolation criterion, by requiring that no more massive halo be located within 30 pMpc, or  $20 r_{200c}$ , whichever is larger, from any re-simulation candidate ( $r_{200c}$  here refers to the radius of the neighbouring, more massive halo). This criterion ensures that our simulations are centred on the peak of the local density structure and not, for example, on a moderately massive halo on the outskirts of an even more massive cluster. Finally, for computational convenience we required that our candidate clusters be no closer than 200 pMpc to any of the periodic simulation box edges.

From this initial list of 91 824 candidate haloes, we then selected a subset of 30 objects for re-simulation. To avoid a bias towards the more common lower-mass haloes, our candidates were binned by  $M_{200c}$  into 10 logarithmic bins from  $10^{14} M_{\odot}$  to  $2 \times 10^{15} M_{\odot}$  ( $\Delta \log_{10} M_{200c} = 0.13$ ). Three objects were then selected from each bin at random. To extend our mass range yet further, we only picked two objects from the highest mass bin, and selected a final halo at even higher mass,  $M_{200c} = 10^{15.34} M_{\odot}$ . These 30 objects comprise the C-EAGLE cluster sample.

### 2.2.2 Motivation for large zoom-in regions

The virial radius, approximated by  $r_{200c}$ , has traditionally been assumed to represent the boundary between a halo and the surrounding Universe, based on the spherical collapse model. However, evidence has emerged in recent years that galaxies might be affected by their environment out to significantly larger distances (e.g. Balogh et al. 1999; Haines et al. 2009; Hansen et al. 2009; von der Linden et al. 2010; Lu et al. 2012; Rasmussen et al. 2012; Wetzel et al. 2012), a result that has been supported by previous generation hydrodynamical simulations (Bahé et al. 2013; Bahé & McCarthy 2015). While most observational evidence for this large-scale influence is based on galaxy colours and SFRs, Bahé et al. (2013) have shown that the GIMIC simulations predict an effect that reaches even further when the hot gas haloes of galaxies are considered instead: in galaxies with  $M_{\text{star}} \approx 10^9 M_{\odot}$ , these are predicted to be depleted even at  $r > 5 r_{200c}$  from the centre of a group or cluster.

Simulations aiming to shed light on the mechanisms affecting galaxy evolution in dense environments should therefore not be limited to the dense cluster haloes alone (within  $\sim r_{200c}$ ), but also extend far enough into the surrounding volume to capture the large-scale environmental impact. The disadvantage of this is a significant increase of the high-resolution simulation volume, increasing both computing time and especially the memory footprint of the simulation. To strike a balance between these conflicting constraints, we simulated 24 of the 30 C-EAGLE clusters with zoom-in regions extending to at least  $10 r_{200c}$  from the cluster centre; these objects



constitute the Hydrangea simulations as analysed in this paper. The remaining six objects, with masses between  $10^{14.6}$  and  $10^{15.2} M_{\odot}$ , were simulated only out to  $5 r_{200c}$ , primarily serving as tools to study the ICM for which each simulation only contributes one (central) object of interest, as opposed to several hundreds or even thousands of galaxies. The additional C-EAGLE simulations are described in more detail by Barnes et al. (2017b).

### 2.2.3 Simulation runs and post-processing

The Hydrangea simulations were run mostly on the HazelHen Cray-XC40 system hosted by the German Federal Maximum Performance Computing Centre (HLRS) at the University of Stuttgart. This system provides nodes with 128 GB of memory each, shared by 24 compute cores for an effectively available 5 GB of memory per core. On this system, we could accommodate most of our hydrodynamic runs on  $\leq 2048$  cores to minimize scaling losses in our highly clustered simulations. From initial conditions (ICs) generated as described in Appendix B (see also Barnes et al. 2017b), the most massive cluster in our sample required more than 10 million core hours to reach  $z = 0$ , corresponding to a total wall clock time of over 10 months (including queueing and downtime). Several clusters from the low-mass end of our sample were run on machines at the Max Planck Computing and Data Facility (MPCDF) in Garching.

In addition to these hydrodynamic simulations, we also performed one DMO simulation of each zoom-in region. These use the same ICs as the hydrodynamical runs, but due to their non-dissipative nature, they produce less small-scale clustering and hence only consumed  $< 10^5$  CPU-hr each.

As main output from the simulations, 30 full ‘snapshots’ were stored between  $z = 14.0$  and  $0$ . Out of these, 28 are spaced equidistant in time ( $\Delta t = 500$  Myr), while two additional snapshots (at  $z = 0.101$  and  $0.366$ ) were included to facilitate comparison to the EAGLE simulations.<sup>5</sup> All snapshots were post-processed with the SUBFIND code (Springel et al. 2001; Dolag et al. 2009) to identify FoF haloes, using a linking length of  $b = 0.2$  times the mean inter-particle separation, and self-bound subhaloes within them. We note in this context that ‘subhalo’ can refer to either the central object that contains the largest fraction of the FoF mass or (where they exist) less massive ‘satellites’.

Subhaloes in the DMO and hydrodynamic runs were individually matched by comparing their unique DM particle IDs, as described by Velliscig et al. (2014) and Schaller et al. (2015a). The 50 most-bound DM particles in each subhalo from the DMO simulation are located in the corresponding hydrodynamic simulation. If one subhalo contains at least half of the particles with the same ID in the hydrodynamic simulation, a link is initiated between the two. This link is then confirmed if, and only if, the original subhalo in the DMO simulation also contains at least 25 of the 50 most-bound DM particles of the corresponding subhalo in the hydrodynamic simulation. 92 per cent of central subhaloes with  $M_{200c} > 10^{11} M_{\odot}$  could be successfully matched between the hydrodynamic and DMO simulations in this way.

To reconstruct the evolutionary and orbital histories of individual simulated galaxies, we have linked subhaloes between different snapshots using an updated version of the algorithm described in

Bahé & McCarthy (2015). This method is described in full in Appendix C. In essence, subhaloes in adjacent snapshots are linked by matching their constituent DM particles, taking into account the formation of new galaxies, mergers between them, and temporary non-identification of galaxies by the SUBFIND algorithm in dense environments (see e.g. Muldrew, Pearce & Power 2011). We note that this algorithm is similar, but not identical, to that used by Qu et al. (2017) to build merger trees from the EAGLE simulations. Unlike in Bahé & McCarthy (2015), we base the tracing on DM particles only. This simplification is possible because of the higher resolution of the Hydrangea simulations, which allows DM haloes to be resolved even for galaxies undergoing severe stripping.

In addition, we stored a larger number of ‘snapshots’ that contain only the most important, and most rapidly time-varying, quantities, such as particle positions and velocities (similar to EAGLE; see Schaye et al. 2015). We stored three snapshots between each of the 28 main snapshots, for a combined time resolution of  $\Delta t = 125$  Myr. This was then additionally boosted to  $\Delta t = 25$  Myr for three 1-Gyr intervals at lookback times of 0–1, 4–5, and 7–8 Gyr. For one intermediate-mass cluster, snapshots were stored at a constant time interval of  $\Delta t = 12.5$  Myr. In future papers, we will exploit the high time resolution provided by these snapshot outputs to trace the evolution of our simulated cluster galaxies in detail; here, we restrict ourselves to an analysis of the snapshot data, in particular those at  $z = 0$  and  $0.101$ .

### 2.2.4 Visualizations of the simulated clusters

A visualization of one Hydrangea simulation is presented in Fig. 1; this contains at its centre the most massive cluster, CE-29, with  $M_{200c} = 10^{15.38} M_{\odot}$ .<sup>6</sup> The main panel shows the gas distribution at  $z = 0$  in a slice of side length  $60 \times 60$  pMpc and thickness 15 pMpc, centred on the potential minimum of the cluster. The colour map, shown in the bottom right inset, encodes both the projected gas density (as brightness) and temperature (as hue/saturation); the coldest gas ( $T \lesssim 10^4$  K) is shown in blue, and the hottest ( $T \gtrsim 10^8$  K) in white. Clearly visible is the central hot ( $T \gtrsim 10^7$  K) halo that extends to  $\sim 4 r_{200c}$ , and a myriad of filaments and embedded haloes out to the nominal edge of our high-resolution region at  $10 r_{200c}$  (thick dotted blue line).

The three panels on the left-hand side present successive zoom-ins towards one individual galaxy on the cluster outskirts, highlighting the vast dynamic range of the simulation. The top two show the gas density and temperature, using the same temperature scaling as the main panel but with adjusted scaling of the surface density for improved clarity. In the bottom panel, we display a synthetic *gri* optical image created with the radiative transfer code ‘SKIRT’ (Camps et al. 2016; Trayford et al. 2017).

The five panels in the bottom row illustrate the formation history of the cluster. Each shows a projected cube of side length  $20 h^{-1}$  cMpc, centred on the main progenitor of the  $z = 0$  cluster. The corresponding physical scale is indicated by the yellow bar in the bottom left corner of each panel, which indicates a length of 1 pMpc. Starting from a web-like structure at  $z \approx 7$ , the simulation forms a number of protocluster cores by  $z = 1.5$  which then successively merge to form the present-day cluster. As an aside, we note that

<sup>5</sup> Including these two extra snapshots, 12 EAGLE snapshots have a counterpart in Hydrangea with a time offset of  $\lesssim 50$  Myr, including eight at  $z \lesssim 2.0$ .

<sup>6</sup> Note that there are small differences between the halo masses in the low-resolution parent simulation and high-resolution hydrodynamic zoom-in re-simulations, by  $< 0.05$  dex. As a convention, we denote individual zoom-in regions, and their central clusters, by the prefix ‘CE’ (for C-EAGLE), followed by their ID number from 0 to 29 (see Table A1).

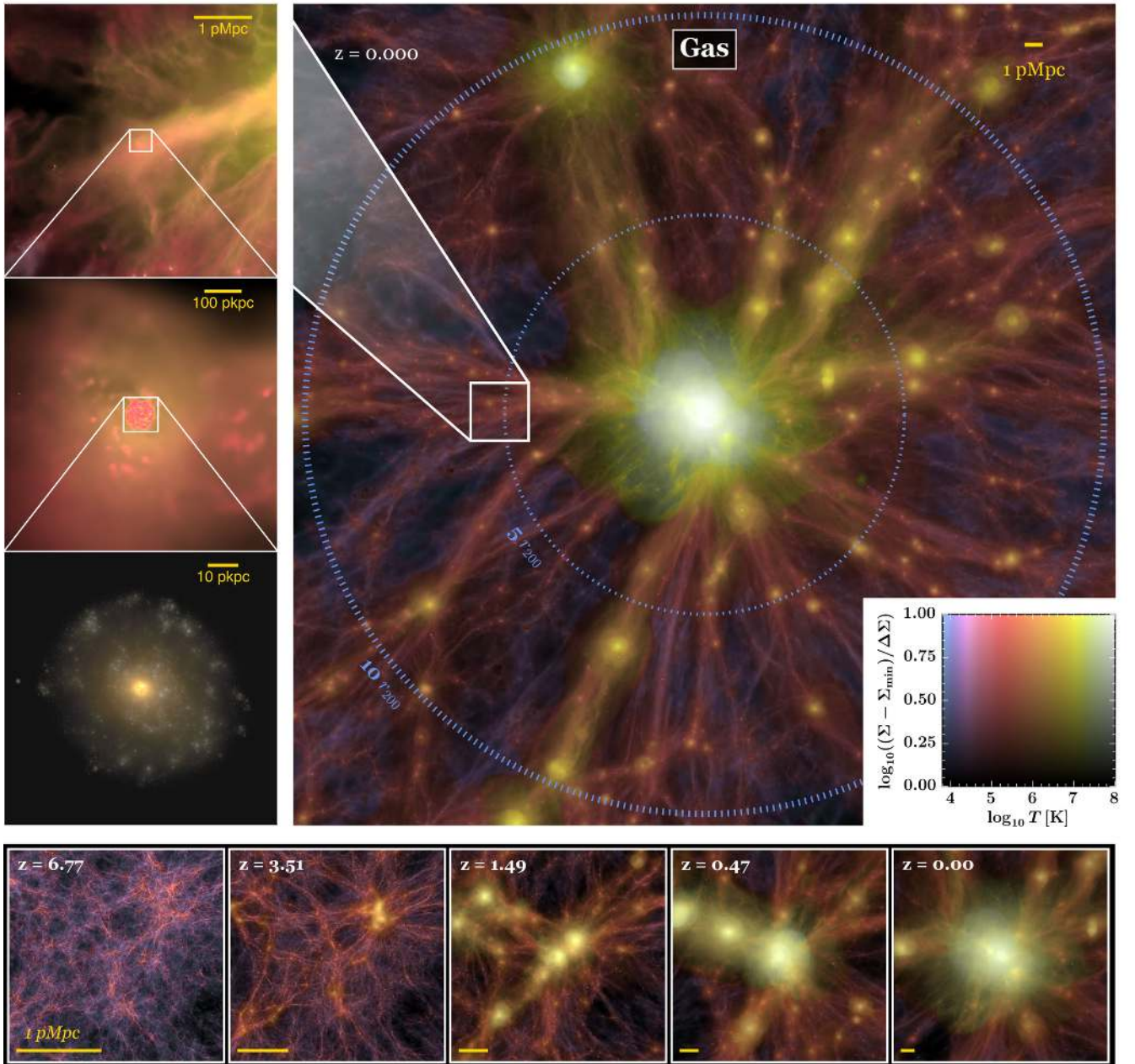


**Figure 1.** Visualization of the gas distribution at redshift  $z = 0$  centred on the most massive Hydrangea cluster (CE-29 with  $M_{200c} = 10^{15.38} M_{\odot}$ ). The main panel presents a  $60 \times 60 \times 15$  pMpc slice centred on the potential minimum of the cluster, with gas surface density and temperature represented, respectively, by the image brightness and hue/saturation (see colour map in the bottom right corner). The two dotted blue rings indicate mid-plane distances of 5 and  $10 r_{200c}$  from the cluster centre; the latter corresponds to the nominal edge of the high-resolution region. The panels on the left-hand side zoom in towards one individual galaxy on the cluster outskirts, highlighting the detailed internal structure that is resolved in our simulations; the bottom panel shows a synthetic optical *gri* image of the galaxy. The five panels in the bottom row show the gas distributions at different redshifts; each is a projected cube with side length  $20 h^{-1}$  cMpc centred on the main progenitor of the  $z = 0$  cluster. For reference, a physical length-scale of 1 pMpc is indicated by the yellow bar in the bottom left corner of each panel.

the main progenitor at high redshift ( $z \gtrsim 1$ ) is clearly not the most massive protocluster core, but the one that experiences the most rapid growth prior to the final merging phase.

The range of cluster morphologies in our suite, on both large and small scales, is illustrated by Fig. 2. For three clusters, this figure shows the gas density and temperature as in Fig. 1, projected within a cube of 30 pMpc side length (top row), and in the bottom row the stellar mass surface density (grey scale) blended with the gas density (purple through yellow) within a cube of 2.5 pMpc side

length. Both are centred on the potential minimum of the cluster. For guidance, the region depicted in the bottom row is indicated by the green box in the top left panel.

The three example clusters are embedded in strikingly different large-scale environments, including a highly isolated object (CE-12, left), a supercluster (CE-22, middle), and a cluster that dominates a region with several less massive haloes (CE-25, right). Similar, but not necessarily correlated, differences are evident in the distribution of galaxies formed from the stars in their centres: some contain a



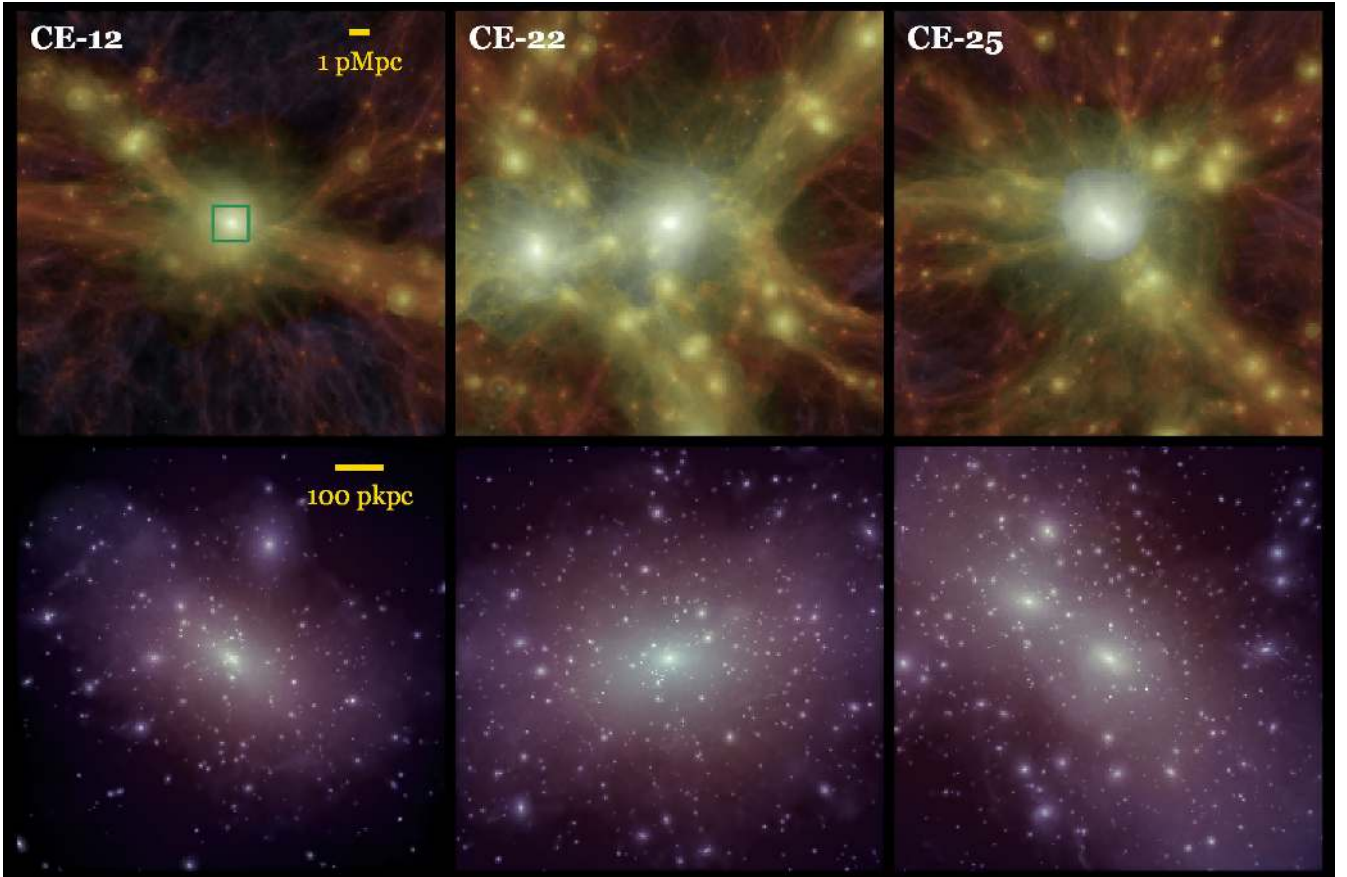


**Figure 2.** Three visual examples of the variety of clusters in the mass range  $4 \times 10^{14} M_{\odot}$ – $1.4 \times 10^{15} M_{\odot}$  in the Hydrangea suite at redshift  $z = 0$ . The top row shows the projected gas density in a 30 pMpc cube with colour indicating the gas temperature as in Fig. 1. The bottom row shows the central 2.5 pMpc of each simulation, with stellar surface density in shades of grey overlaid on gas density (purple through yellow). The green box in the top left panel indicates the size of the regions depicted on the bottom row.

dominating ‘brightest cluster galaxy’ (BCG; e.g. CE-12 and CE-22), whereas CE-25 in the right-hand column is currently undergoing a triple merger without an obvious ‘central’ galaxy.<sup>7</sup>

Fig. 3 presents an overview of the distribution of the central C-EAGLE clusters in mass–concentration space, where concentrations  $c \equiv r_{200c}/r_s$  were obtained by fitting an NFW profile with scale radius  $r_s$  to the spherically averaged DM distribution between  $r = 0.05$  and  $1 r_{200c}$  (Neto et al. 2007; Schaller et al. 2015b), centred on the potential minimum of the cluster. Clusters that are ‘relaxed’ (i.e. with an offset between the centre of mass and centre of potential,  $s$ , less than  $0.07 r_{200c}$  and a substructure fraction of less than 0.1; Neto et al. 2007) are shown as circles, unrelaxed haloes that violate one or both of these criteria as stars. Clusters from the Hydrangea sample (i.e. those with high-resolution regions extending to  $10 r_{200c}$ ) are represented by filled symbols, the six remaining C-EAGLE clusters by open symbols. In qualitative agreement with the findings of e.g. Neto et al. (2007), unrelaxed clusters are typically less concentrated than similarly massive relaxed ones. With significant scatter, the C-EAGLE clusters follow the well-known trend towards lower concentration at higher mass, consistent with the trend from the large DMO simulation in the Planck  $\Lambda$ CDM cosmology of Dutton & Macciò (2014).

<sup>7</sup> As can be seen in the top panel, this merger leads to an expansion of the hot halo in a clear shock front.

We also indicate the formation time of each cluster, defined as the lookback time when the main progenitor of the cluster assembled half its present-day mass, as the colour of each point. As expected, there is a strong correlation between age and mass in the sense that less massive clusters assembled earlier. A second, albeit less strong, correlation exists between concentration and formation time (less concentrated clusters having typically formed somewhat more recently). In future work, we will exploit this diversity of our cluster sample to investigate in detail the impact of these differences on the galaxy population. Table A1 in Appendix A lists the best-fitting concentrations along with other information on the mass, position, and environment of all the C-EAGLE clusters.

In combination, the 24 Hydrangea regions contain, at  $z = 0$  and within  $10 r_{200c}$  from the centre of their main halo, 24 442 galaxies with  $M_{\text{star}} \geq 10^9 M_{\odot}$ , and 7207 with  $M_{\text{star}} \geq 10^{10} M_{\odot}$ . We note that this exceeds the corresponding numbers in the 100 cMpc EAGLE reference simulation by a factor of  $\gtrsim 2.5$ , as a consequence of the larger (combined) simulation volume and the higher galaxy density in our simulated clusters.

### 3 STELLAR MASSES AND QUENCHED FRACTIONS OF SIMULATED CLUSTER GALAXIES

We begin our analysis of the Hydrangea simulations by comparing their predictions for two fundamental galaxy properties to

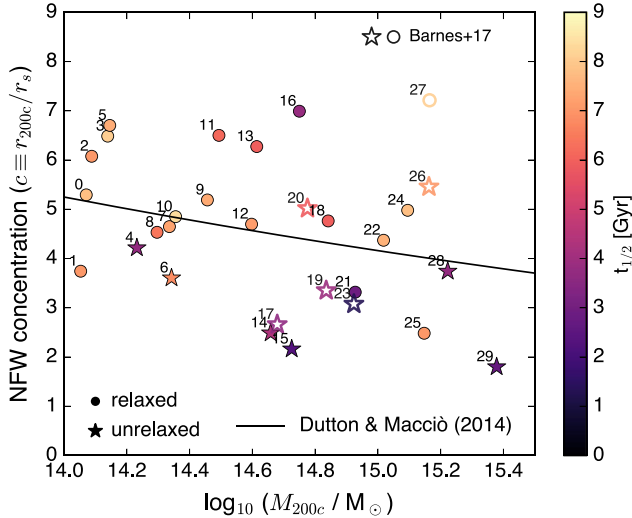


**Figure 3.** Mass–concentration relation of the C-EAGLE clusters at redshift  $z = 0$ . The 24 Hydrangea clusters are shown as filled symbols, colour indicating the lookback time when the cluster assembled half its present-day mass,  $t_{1/2}$ . The additional six clusters introduced by Barnes et al. (2017b) are shown as empty symbols. Concentration is defined as  $c \equiv r_{200c}/r_s$ , where  $r_s$  is the best-fitting NFW scale radius. Relaxed clusters are shown with circles, unrelaxed ones with star symbols (see the text for details). The sample spans a wide range in mass, concentration, dynamical state, and assembly histories.

observations, namely their stellar masses (Section 3.1), and quenched fractions (Section 3.2). We restrict ourselves to comparisons to observations at  $z \approx 0$ , and will test the simulation predictions at higher redshift in future work. Because the observational studies, we are comparing to are focused on the central cluster regions, we include in this section also the six additional C-EAGLE clusters from Barnes et al. (2017b) whose high-resolution regions extend only to  $5 r_{200c}$ .

### 3.1 Galaxy stellar masses

The stellar mass of a galaxy is one of its most fundamental characteristics, and many other properties have been shown to correlate strongly with stellar mass: e.g. colour, SFR (e.g. Kauffmann et al. 2003b; Wetzel et al. 2012), metallicity (e.g. Tremonti et al. 2004; Gallazzi et al. 2005; Sánchez et al. 2013), and, for centrals, their halo mass (e.g. White & Rees 1978). We now test the galaxy masses predicted by our simulations against observations, for both central cluster galaxies (‘BCGs’) and their satellites.

#### 3.1.1 BCG and halo stellar masses

In Fig. 4, we show both the total stellar mass of the clusters in our simulations (i.e. the mass of all star particles within  $r_{3D} = r_{500c}$ , the radius within which the average density equals 500 times the critical density; left-hand panel), and the stellar mass of the BCG, i.e. the galaxy at the potential minimum of the cluster’s FoF halo, in the right-hand panel (integrated within a circular aperture with  $R_{2D} = 50$  pkpc, see below). Both are shown as a function of total halo mass, which is quantified as  $M_{500c}$  in the left-hand panel, but as  $M_{200c}$  in the right-hand panel. Predictions from our simulations are shown in shades of green, dark for the 30 central clusters (i.e. the most massive ones in their simulation volume), and light green for others. Observational data are shown in grey. For halo stellar masses, we

compare to the observations of Gonzalez et al. (2013) and Kravtsov, Vikhlinin & Meshcheryakov (2014), and the best-fitting relation derived from SDSS images by Budzynski et al. (2014). In the observations,  $M_{500c}$  is estimated from the X-ray temperature (Gonzalez et al. 2013; Kravtsov et al. 2014) and the mass-richness relation (Budzynski et al. 2014); we multiply these with a factor of 1.5 to convert from  $M_{500c}$  to  $M_{200c}$ . In the simulations, we measure halo masses directly (masses derived from mock X-ray spectra are presented in Barnes et al. 2017b). All measurements of the total stellar mass in the halo in the left-hand panel include contributions from intracluster light, in both the simulations and observations. We note that the first two observational data sets are from clusters at  $z \lesssim 0.1$ , whereas the Budzynski et al. (2014) relation was derived for clusters at  $0.15 \leq z \leq 0.4$ . We here compare to the simulation output at  $z = 0.101$  as a compromise between these two ranges.

We first consider the simulation prediction for the 30 central clusters (dark green stars in Fig. 4), which exhibit a fairly tight relation between halo mass and both the halo and BCG stellar mass. The former is slightly sublinear (best-fitting power law index  $\alpha = 0.86 \pm 0.05$ , with a best-fitting overall stellar fraction of 1.51 per cent). This is less steep than the relation of Budzynski et al. (2014),  $\alpha = 1.05 \pm 0.05$ , but slightly steeper than in Gonzalez et al. (2013) and Kravtsov et al. (2014). A sublinear scaling between the stellar and halo mass of galaxy clusters was also reported by Andreon (2010). We therefore conclude that, overall, the (central) C-EAGLE clusters have formed approximately realistic amounts of stellar mass (see also Barnes et al. 2017b).

The agreement is less good when only the stellar mass of the BCG is considered, which we define as the mass within a (2D) radial aperture of 50 pkpc and integrating through the entire high-resolution simulation region along the line of sight (right-hand panel of Fig. 4). Stott et al. (2010) have shown that this aperture mimics the Kron (1980) aperture commonly encountered in observational analyses, including that of Bellstedt et al. (2016) whose BCG stellar mass measurements (at  $z < 0.2$ , and including the measurements of Lidman et al. 2012 used by these authors) we show as light grey circles. Also shown are BCG masses from Kravtsov et al. (2014), measured within a projected radius of 50 pkpc, and those of Gonzalez et al. (2013), corrected to  $R_{2D} \leq 50$  pkpc by multiplying with a correction factor of 0.4 (see Gonzalez, Zabludoff & Zaritsky 2005).

The stellar masses of the simulated central BCGs (dark green) lie significantly above all these data sets, by  $\sim 0.3$  dex compared to Gonzalez et al. (2013) and Kravtsov et al. (2014), and  $\sim 0.6$  dex compared to Bellstedt et al. (2016). This discrepancy is greatest for the most massive haloes. In the companion paper of Barnes et al. (2017b), we demonstrate that – despite the use of the AGNdt9 model that alleviated the unrealistically high gas mass fractions in group haloes – our clusters also have a hot gas fraction that is somewhat too high compared to what is inferred from X-ray observations. Correspondingly, the SFRs of the central cluster galaxies within the central 15 pkpc (not shown) are all in the range from  $\sim 1$  to  $\sim 10 M_\odot \text{ yr}^{-1}$ , whereas only  $\lesssim 50$  per cent of observed central cluster galaxies show evidence for star formation at this level (e.g. Hoffer et al. 2012; Donahue et al. 2015; Fogarty et al. 2015). It is tempting to identify this excess star formation as the cause of the unrealistically high BCG masses. However, only  $\sim 10$  per cent of the mass of our simulated BCGs has typically been formed at  $z < 1$ . The BCG masses are therefore not predominantly too high because of artificially high levels of in situ star formation at low redshift, but reflect a shortcoming of the simulations in modelling their high-redshift protocluster progenitors.



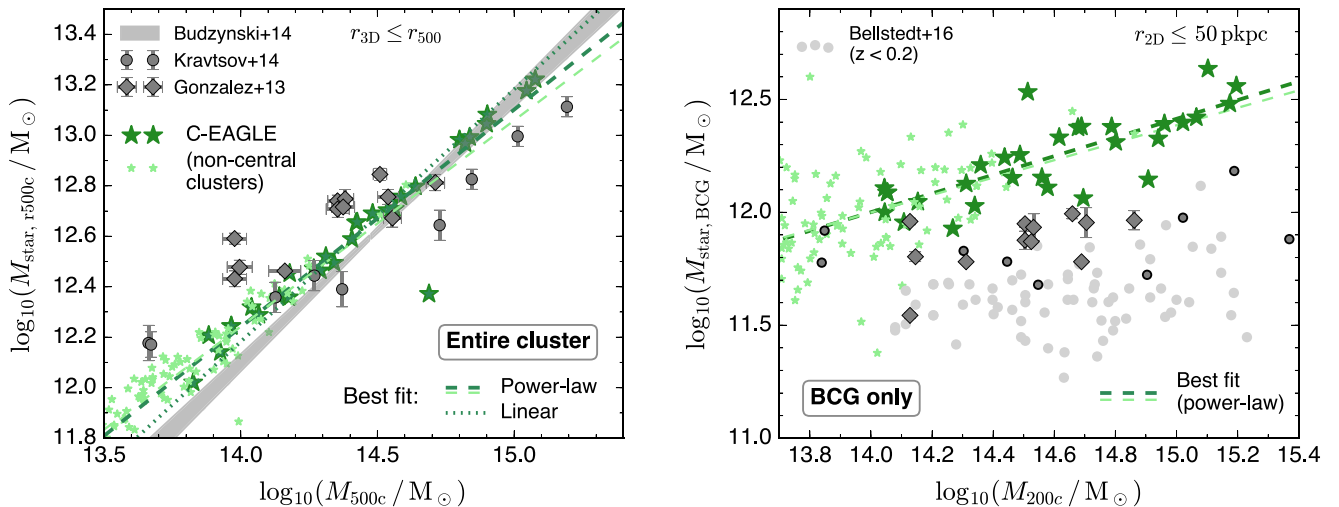


**Figure 4.** *Left:* stellar mass of C-EAGLE clusters within  $r_{500c}$  (green stars) as a function of true halo mass, compared to several observational data sets (grey points and band). Large dark green symbols represent the 30 central clusters within each simulation, other clusters within the simulation volume (with  $M_{200c} \geq 5 \times 10^{13} M_{\odot}$ ) are shown as small light green stars. *Right:* stellar mass of the simulated BCGs as a function of halo mass, measured within a circular aperture of  $R_{2D} < 50$  pkpc, compared to observations. In both panels, dashed dark green lines show the best power-law fit to the simulated relation for central clusters with slopes of  $\alpha = 0.86 \pm 0.05$  (within  $r_{500c}$ ) and  $\alpha = 0.41 \pm 0.06$  (for the BCGs); thin light green lines show the analogous fits for non-central clusters. In the left-hand panel, the dotted dark green line additionally shows the best linear fit, corresponding to a stellar fraction of 1.51 per cent. Although the total mass of stars in the halo (within  $r_{500c}$ ) is reproduced well by the simulations, BCGs are too massive by a factor of  $\sim 3$ . Non-central (‘secondary’) clusters follow the same relation as their central counterparts.

Unrealistically massive central cluster galaxies have also been a common feature of many previous simulations. In the earliest cases, this was a consequence of including no feedback, or only stellar feedback which becomes ineffective at regulating star formation in haloes above  $M_{200c} \approx 10^{12} M_{\odot}$  (see Balogh et al. 2001 and references therein). During the last decade, these discrepancies have motivated the inclusion of AGN feedback in simulations, which alleviates this ‘overcooling problem’ in groups and clusters (e.g. Sijacki et al. 2007; Fabjan et al. 2010; McCarthy et al. 2010; Gaspari, Brighenti & Ruszkowski 2013), primarily by expelling gas from their progenitors at  $z \approx 2-4$  (McCarthy et al. 2011). However, in line with our findings from Fig. 4, a number of studies in recent years have shown that even the inclusion of AGN feedback models can still lead to predicted present-day SFRs, stellar masses, and hot gas fractions of massive haloes that are higher than observed (e.g. Fabjan et al. 2010; Ragone-Figueroa et al. 2013; Vogelsberger et al. 2014; Schaye et al. 2015; see also Scannapieco et al. 2012). It is likely that the resolution of this longstanding problem will require the development of less simplistic AGN feedback models that are more efficient at expelling gas from massive haloes at high redshift.

To judge the effect of overly massive BCGs on the predicted relation between stellar mass within  $r_{500c}$  and  $M_{500c}$  (left-hand panel), we have also computed cluster stellar masses excluding a sphere of radius 50 pkpc around the cluster centre (for clarity, this is not shown in Fig. 4). Because the relation between BCG mass and halo mass is strongly sublinear (see right-hand panel of Fig. 4), this correction does not affect clusters with  $M_{500c} > 10^{14.4} M_{\odot}$ . In lower-mass clusters, excluding the centre completely – which is clearly an overcorrection, since the C-EAGLE BCG masses at the low-mass end are only too high by a factor of  $\sim 2$  – reduces the stellar mass by up to 0.2 dex and shifts the C-EAGLE predictions on the relation of Budzynski et al. (2014). On a qualitative level, the excess mass in our simulated BCGs does therefore not affect our conclusion that the total stellar mass in the C-EAGLE clusters is consistent with observations.

Due to their large volume, the Hydrangea simulations also contain a large number of ‘secondary’ cluster haloes that are less massive than the ‘primary’ one at the centre of each simulation. In total, there are 38 of these with  $M_{200c} > 5 \times 10^{13} M_{\odot}$  within 10 (5)  $r_{200c}$  from the central cluster in the Hydrangea (other C-EAGLE) simulations. This number is boosted to 81 when including objects beyond this nominal edge of the high-resolution sphere, but which are still far away ( $> 8$  pMpc) from any low-resolution boundary particles.<sup>8</sup> At fixed  $M_{500c}$ , secondary clusters (light green stars in Fig. 4) contain the same stellar mass as primaries, both within  $r_{500c}$  and in their BCG.

### 3.1.2 The stellar mass function of satellite galaxies

We now compare the simulation predictions for the low-redshift satellite GSMF. This has been studied observationally by several authors in recent years, including Yang et al. (2009, based on SDSS spectroscopic data and the Yang et al. 2007 SDSS halo catalogue), Vulcani et al. (2011, from the WINGS survey of nearby galaxy clusters), and Wang & White (2012, again from SDSS data but stacking galaxy counts around bright isolated galaxies).

All three of these observational studies exclude BCGs, but each uses a somewhat different definition of ‘satellite galaxy’. We therefore begin by briefly describing these different selections and our methods for approximating them within the C-EAGLE simulations.

Yang et al. (2009) used the Yang et al. (2007) halo catalogue to match SDSS galaxies to underlying DM haloes based on their spatial distribution. The most massive galaxy in each halo is

<sup>8</sup> These ‘external’ secondary clusters can exist because the high-resolution regions at  $z \approx 0$  are, in general, non-spherical. We have verified that they do not display any significant difference in their stellar masses from secondary clusters within the nominal high-resolution region.

identified as ‘central’, while all others are ‘satellites’. These authors report the satellite GSMF for different bins of halo mass, out of which we here compare to the (most massive) bin with  $14.4 \leq \log_{10} M_{200c}/(h^{-1} M_{\odot}) < 14.7$ . There are seven C-EAGLE clusters in this mass range, for which we select all simulated galaxies that SUBFIND identifies as satellites of the cluster FoF halo.

Vulcani et al. (2011) assigned cluster membership in the WINGS catalogue (Fasano et al. 2006) based on 2D projected distance from the cluster centre ( $R_{2D} \leq 0.6 r_{200}$ ). The WINGS clusters have  $M_{200c} \gtrsim 10^{14.5} M_{\odot}$  (Fasano et al. 2006).<sup>9</sup> We therefore compare to the 17 C-EAGLE clusters with  $M_{200c} \geq 10^{14.5} M_{\odot}$  and select those galaxies within  $R_{2D} \leq 0.6 r_{200c}$  from the potential minimum of each cluster.<sup>10</sup>

Wang & White (2012) used a fixed 300 pkpc aperture around bright isolated galaxies to count satellites, but even in their highest stellar mass bin, the typical halo mass (as estimated from semi-analytic models) is only  $\sim 10^{13.7} M_{\odot}$ . This is slightly lower than the halo mass range of our simulations, so we compare to simulated haloes in the mass range  $14.0 \leq \log_{10} M_{200c}/M_{\odot} < 14.5$  (13 clusters) and re-normalize the Wang & White (2012) GSMF as described below.

Besides differences in galaxy selection, the observations span a range of redshifts, with median  $z \approx 0.1$  for SDSS (Yang et al. 2009; Wang & White 2012), while the WINGS clusters lie at  $0.04 < z < 0.07$  (Vulcani et al. 2011). For simplicity, we compare all three data sets to the simulation predictions at  $z = 0.101$ , but have verified that differences to the predictions at  $z = 0$  are small. In all three cases, we compute stellar masses in the simulations as the sum of all gravitationally bound star particles that are within 30 pkpc from the potential minimum of their subhalo. Schaye et al. (2015) have shown that this aperture yields a good match to the Petrosian apertures often employed in observations, including those from the SDSS. We restrict our comparison here to the primary (central) clusters of each simulation.

The comparison between simulations and observational data is shown in Fig. 5. The simulated GSMF is shown with solid lines where bins contain more than 10 galaxies, and dashed lines for more sparsely sampled bins at the high stellar mass end. The observations are shown as empty symbols, with error bars indicating the observational  $1\sigma$  uncertainties. Data points for WINGS (green) and Wang & White (2012) have been scaled by multiplying their stellar mass function with a correction factor such that the total number of galaxies above a given threshold ( $M_{\text{star}} = 10^{9.8} M_{\odot}$  for WINGS,  $10^{9.4} M_{\odot}$  for Wang & White 2012) is the same as in the C-EAGLE simulations. In the case of WINGS, this is necessary because the GSMF presented by Vulcani et al. (2011) has been scaled for the purpose of comparing to field galaxies, while the GSMF of Wang & White (2012) was derived for haloes that are less massive than the C-EAGLE sample (see above); the correction factor applied to this data set is equal to 1.50. Differently coloured lines correspond to simulated GSMFs matched to the correspondingly coloured observational data set, as described above.

<sup>9</sup> We have used the  $L_X$ – $M_{500c}$  relation of Vikhlinin et al. (2009) to convert the WINGS X-ray luminosities of Fasano et al. (2006) to halo masses, with an additional correction factor of 1.5 to convert to  $M_{200c}$ .

<sup>10</sup> We have not imposed an additional cut along the line of sight, because the criterion of  $\Delta z \leq 3\sigma$  (with redshift  $z$  and cluster velocity dispersion  $\sigma$ ) of Vulcani et al. (2011) corresponds to an integration length that is comparable to the size of the high-resolution region in our simulations.

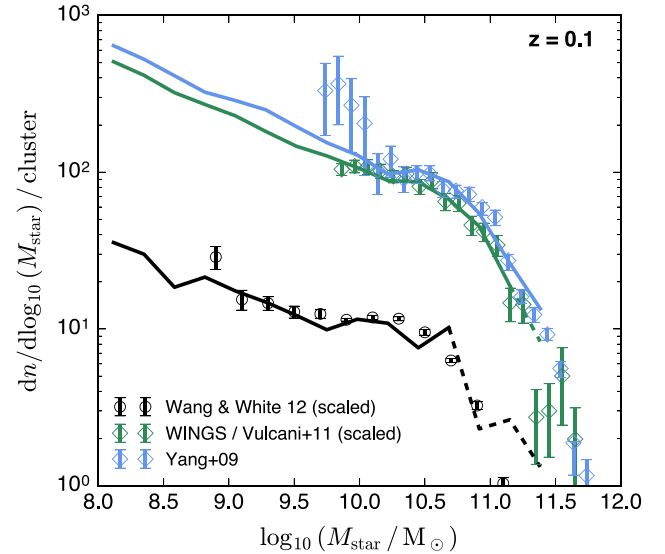


**Figure 5.** Galaxy stellar mass function (GSMF) at  $z = 0.101$  for satellites in the C-EAGLE simulations (solid lines, dashed where there are  $< 10$  galaxies per 0.25 dex bin) compared to observations (open diamonds). The three different lines represent galaxy selections approximately matched to the respectively coloured observational survey:  $14.0 \leq \log_{10}(M_{200c}/M_{\odot}) < 14.5$ ,  $R_{2D} < 300$  pkpc (black);  $14.5 \leq \log_{10}(M_{200c}/M_{\odot})$ ,  $R_{2D} < 0.6 r_{200c}$  (green);  $14.4 \leq \log_{10} M_{200c}/(M_{\odot} h^{-1}) < 14.7$ , all halo members (blue). Overall, the simulations achieve an excellent match to the observations.

Overall, the simulated  $z \approx 0$  GSMF agrees well with all three data sets. The only slight tension is seen at the low-mass end of the Wang & White (2012) and Yang et al. (2009) comparisons, where the observations hint at an upturn of the GSMF that is not seen in the simulations. We note that these observational data points also have large uncertainties – in the case of Yang et al. (2009), the discrepancy for an individual data point is only significant at the  $\sim 1\sigma$  level – but alternatively, this deficiency might be a consequence of overly efficient star formation quenching in low-mass galaxies in our simulations, as we shall discuss shortly.

The accuracy of the predicted cluster GSMF reflects, in part, the calibrated match between the EAGLE simulations and the field GSMF (Schaye et al. 2015). However, as shown below, there are significant differences between the field and cluster GSMF in our simulations. The close agreement between our cluster GSMF and the observations shown in Fig. 5 therefore suggests a realistic modelling of cluster-specific aspects of galaxy formation, at least to the extent that they manifest themselves in the stellar mass of galaxies. We exploit this success of our simulations further in Section 4, where we compare the GSMF in and around simulated clusters to the field.

### 3.2 Satellite quenched fractions

A second key property of galaxies, which is closely related to their stellar mass, is their SFR. Observations have shown conclusively that galaxies in dense environments are biased towards lower specific star formation rates ( $sSFR \equiv SFR/M_{\text{star}}$ ; e.g. Kauffmann et al. 2004), with the key difference being an increased fraction of passive galaxies (e.g. Peng et al. 2010; Wetzel et al. 2012). We now test the C-EAGLE predictions for the quenched fraction of simulated satellites.

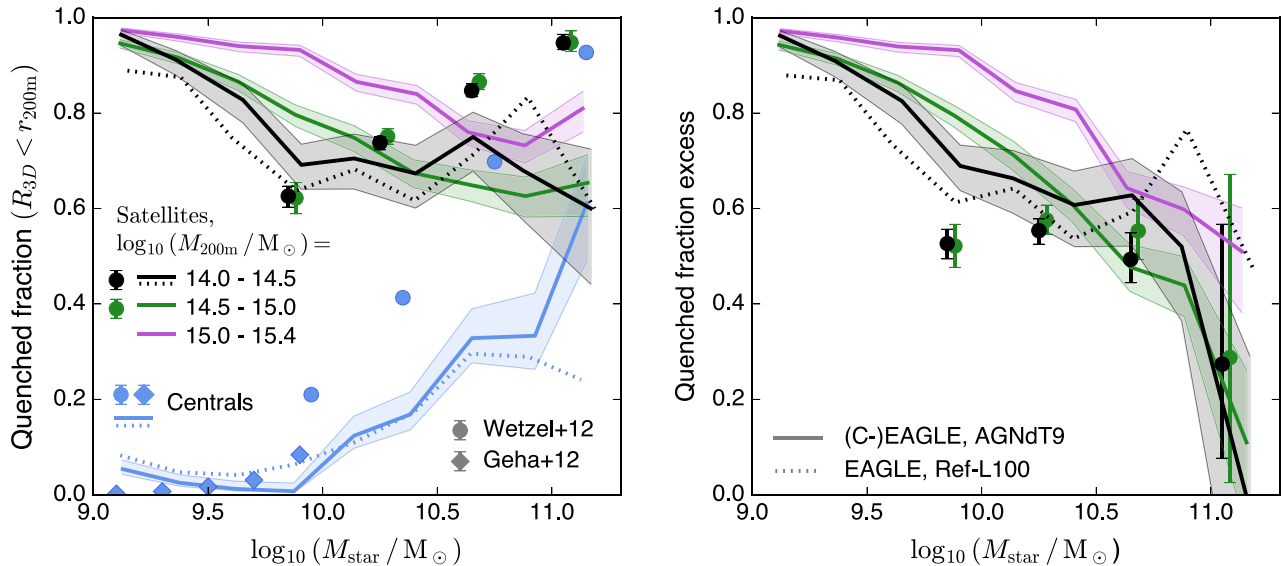


**Figure 6.** *Left:* quenched satellite fraction within  $r_{3D} \leq r_{200m}$ , in bins of cluster mass (differently coloured solid lines) as a function of stellar mass. The blue solid line shows the corresponding trend in the field, i.e. centrals in the AGNdT9-L050 simulation from the EAGLE suite. Shaded bands indicate  $1\sigma$  binomial uncertainties (Cameron 2011). The dotted blue and black lines are the corresponding trends from the EAGLE Ref-L100 simulation. Filled circles with error bars show the corresponding values from the SDSS DR7 analysis of Wetzel et al. (2012) and blue diamonds the observed quenched fractions of field dwarfs from Geha et al. (2012). In agreement with observations, simulated satellites show an enhanced quenched fraction compared to the field, albeit with discrepancies in the trends with  $M_{\text{star}}$  (see the text for details). *Right:* the satellite quenched fraction excess,  $(f_q^{\text{sat}} - f_q^{\text{cen}})/(1 - f_q^{\text{cen}})$ , which shows quantitative agreement between simulations and observations at  $M_{\text{star}} > 10^{10} M_{\odot}$ .

In the left-hand panel of Fig. 6, we show the passive fraction of C-EAGLE cluster satellites as a function of stellar mass and host mass. For consistency with the observational analysis of Wetzel et al. (2012), we define ‘passive’ galaxies as those with  $\text{sSFR} < 10^{-11} \text{ yr}^{-1}$ . For the same reason, we take cluster mass here as  $M_{200m}$  (the mass within the radius  $r_{200m}$  inside which the average density is 200 times the *mean*, as opposed to critical, density of the Universe) and select as satellites those galaxies at radii  $r_{3D} \leq r_{200m}$  (excluding the BCG).<sup>11</sup>

Clusters are grouped into three mass bins between  $M_{200m} = 10^{14}$  and  $10^{15.5} M_{\odot}$ , represented by different colours. For comparison, we also show the corresponding quenched fraction of central galaxies from the EAGLE AGNdT9-L050 simulation (which was run with the exact same simulation parameters as C-EAGLE; solid blue line). Shaded bands indicate the statistical binomial  $1\sigma$  uncertainty (Cameron 2011) on the quenched fraction. Observational data from Wetzel et al. (2012) are overlaid as filled circles in corresponding colours; the error bars represent  $1\sigma$  uncertainties. We note that their observations do not probe the highest halo mass bin (purple). Also plotted are the quenched fractions of low-mass field galaxies from Geha et al. (2012, blue diamonds). Finally, the analogous trends from the EAGLE Ref-L100 simulation – whose parameters describing AGN feedback are different from C-EAGLE, see Section 2.1 – are shown as dotted lines, both for centrals (blue) and the lowest-mass cluster bin (black).

The dominant feature of Fig. 6 is an increased quenched fraction of satellites across the range of halo masses shown here ( $M_{200m} > 10^{14} M_{\odot}$ ), at least at  $M_{\text{star}} < 10^{11} M_{\odot}$ , which agrees

qualitatively with observations. Similar to what is seen in the Wetzel et al. (2012) data, the quenched fractions in the 14.0–14.5 and 14.5–15.0 halo mass bins (black/green) closely follow each other. For the nine clusters with  $M_{200m} > 10^{15} M_{\odot}$ , the simulations predict a substantially higher quenched fraction, especially at intermediate stellar masses ( $M_{\text{star}} \approx 10^{10} M_{\odot}$ ).

In contrast both to observations and to simulated central galaxies, the quenched fractions of simulated cluster satellites do not show an increase with stellar mass. On the contrary, they show a decrease, especially at  $M_{\text{star}} \lesssim 10^{10} M_{\odot}$ . The quenched satellite fraction in the C-EAGLE simulations at  $M_{\text{star}} \gtrsim 10^{10} M_{\odot}$  is therefore lower than observed. This discrepancy is most severe for the most massive galaxies ( $M_{\text{star}} \approx 10^{11.5} M_{\odot}$ ; 70 per cent in C-EAGLE versus near 100 per cent in the data). We point out, however, that even for *central* galaxies, in both the EAGLE AGNdT9 and Ref runs (blue solid and dotted lines), the massive quenched fractions are under-predicted, which points to a more fundamental discrepancy between the simulations and observations, for example because quenching due to internal mechanisms such as AGN (see e.g. Bower et al. 2017) is not efficient enough in the EAGLE model. Alternatively, the quenched fractions in the observations may be overestimated, as demonstrated by Trayford et al. (2017) in the case of quenched fractions derived from galaxy colours. However, the quenched fractions of Wetzel et al. (2012) are derived from optical spectra and not colours, and a recent study by Chang et al. (2015) found that these tend to *overestimate* SFRs, which would exacerbate rather than alleviate the discrepancy. To isolate the *environmental* impact on the quenched fraction, we plot in the right-hand panel of Fig. 6 the ‘quenched fraction excess’, defined as  $(f_q^{\text{sat}} - f_q^{\text{cen}})/(1 - f_q^{\text{cen}})$  as proposed by Wetzel et al. (2012). In this metric, the simulations show much closer agreement with the observations, indicating that the environmental impact on star-forming gas is modelled correctly in our simulations, at least for  $M_{\text{star}} > 10^{10} M_{\odot}$ .

<sup>11</sup> The group finding algorithm of Wetzel et al. (2012) accounts for line-of-sight projection in a probabilistic way, with the aim of assigning galaxies to haloes in 3D space. We have repeated the analysis presented here with a cut in  $R_{2D}$  instead, and found no qualitative differences.



At lower stellar masses ( $M_{\text{star}} \lesssim 10^{10} M_{\odot}$ ), observations indicate a continued decrease in the passive fraction of both satellites and centrals with decreasing stellar mass (Geha et al. 2012, blue diamonds in Fig. 6). While this is approximately reproduced by EAGLE centrals – whose passive fraction is  $<10$  per cent at  $M_{\text{star}} = 10^9 M_{\odot}$  – the passive fraction of satellites in our simulations *increases* significantly, and almost reaches unity at  $M_{\text{star}} = 10^9 M_{\odot}$ , independent of host mass. In Schaye et al. (2015), it was already shown that EAGLE predicts a passive fraction in the combined galaxy population (centrals and satellites) that rises towards lower stellar masses below  $M_{\text{star}} \approx 10^{9.5} M_{\odot}$ , and that this effect is strongly resolution dependent. Because almost all these quenched low-mass galaxies are satellites (at least down to  $M_{\text{star}} = 10^9 M_{\odot}$ , see our Fig. 6), the overefficient quenching of low-mass satellites in C-EAGLE can therefore also be primarily ascribed to resolution effects, even though all galaxies shown here are resolved by  $\gg 1000$  particles.

We speculate that this effect may be connected to the overly porous structure of atomic hydrogen discs in many EAGLE galaxies reported by Bahé et al. (2016). As a consequence of limited resolution, star formation feedback events in the EAGLE model create holes that are larger than observed, and it is possible that this increased porosity might make the disc more susceptible to being stripped under the influence of ram pressure.

As a final note, we emphasize that an artificial increase in the passive (or red) fraction of low-mass satellites with decreasing stellar mass is not unique to our simulations, and has also been described by many other authors. This includes hydrodynamical simulations with a fundamentally different treatment of hydrodynamics and stellar feedback (Vogelsberger et al. 2014) as well as semi-analytic models (e.g. Guo et al. 2013; Henriques et al. 2013). As well as improved resolution and more sophisticated feedback recipes, the generation of low-mass satellite galaxies with realistically low quenched fractions may therefore also require other changes to the simulation model, e.g. in the treatment of the star-forming interstellar medium (ISM).

## 4 ENVIRONMENTAL INFLUENCE ON STELLAR MASSES

We have shown in the previous section that the C-EAGLE simulations produce realistic satellite galaxy stellar mass distributions in the cores of massive clusters, while the underlying EAGLE model reproduces, by construction, the GSMF in the field (Schaye et al. 2015; Crain et al. 2015). This gives the simulations power to gain theoretical insight into how environment affects the GSMF in and around clusters. We will now proceed with a first analysis of these environmental effects. For consistency with the previous section and SDSS-based observations (see Schaye et al. 2015), we continue to only consider stars within 30 pkpc from the potential minimum of each galaxy’s subhalo. Despite some difference in detail, none of our findings below change qualitatively when including all stars bound to the subhalo instead.

### 4.1 Environmental impact on the normalized stellar mass function

A key difficulty of comparing GSMFs between different environments is the application of a suitable normalization, since by definition the overall density of galaxies is higher in clusters than in the field. In the observational literature this has, for instance, been accomplished by re-normalizing cluster and field mass functions so both yield the same total number of galaxies above a given mass

limit (e.g. Vulcani et al. 2011). In our simulations, a more natural way to accomplish this is to divide the number of galaxies by the *total mass* within the same volume, effectively computing the bias of galaxies of different mass with respect to the general mass distribution as in Crain et al. (2009).

We present this comparison in Fig. 7, where we show the normalized GSMF, i.e.  $\phi \equiv dn/d\log_{10} M_{\text{star}} / (M_{\text{tot}}/10^{10} M_{\odot})$ , where  $M_{\text{tot}}$  is the total mass within the volume that galaxies are selected from. We distinguish between Hydrangea clusters in three different mass bins (different panels, increasing from left to right). For each bin, we stack all clusters and extract the GSMF in three concentric shells centred on the cluster’s potential minimum, in the radial range  $r = 0$ – $r_{200c}$  (the virialized central region),  $1$ – $5 r_{200c}$  (the region comprising a mix of first-infall and backsplash galaxies; see Bahé et al. 2013), and  $5$ – $10 r_{200c}$  (the primordial infall region). For comparison, we also show the normalized GSMF from the EAGLE AGNdt9-L050 (blue) and Ref-L100 (purple) periodic-box simulations. Since these model representative cosmic volumes, they can be taken as estimates of the ‘field’ GSMF. There is very close agreement between these latter two distributions (Schaye et al. 2015), with the key difference being that Ref-L100 extends to higher masses due to its eight times larger volume.

At first sight, the normalized stellar mass function shows little difference between the different environments, with particularly close agreement at  $M_{\text{star}} \approx 10^{10} M_{\odot}$  in all three halo mass bins. On closer inspection, however, there are two clear and significant differences. First, there is a deficiency of low stellar mass galaxies ( $M_{\text{star}} \lesssim 10^{10} M_{\odot}$ ) within  $r_{200c}$  (red line), of up to  $\sim 0.2$  dex. Secondly, massive galaxies ( $M_{\text{star}} \gtrsim 10^{10.5} M_{\odot}$ ) are more numerous in our simulated clusters, from the central region ( $< r_{200c}$ ) to the far outskirts (the  $5$ – $10 r_{200c}$  zone; yellow). Qualitatively, this is consistent with the recent Dark Energy Survey analysis of Etherington et al. (2017), who found a higher fraction of massive galaxies in higher density environments. The bottom panels show the mass functions normalized to Ref-L100 to bring out these differences more clearly. Over more than a decade in halo mass, the environmental differences in galaxy stellar mass show no strong dependence on cluster mass.

The deficiency of low-mass galaxies within the virial radius can be due to tidal stripping (or even complete disruption) of satellites, lack of stellar mass growth as a result of star formation quenching, or a combination thereof. In Fig. 8, we test these hypotheses by constructing GSMFs separately for young and old stars, defined as those formed after or before redshift  $z = 1$ , respectively. The environmental impact on these two different populations is strikingly different. From the left-hand panel, the young stellar mass function shows a strong deficiency at the low-mass end (by up to 0.4 dex), but only a minor high-mass excess except for the most massive galaxies ( $M_{\text{star,young}} > 10^{11} M_{\odot}$ ). From the horizontal offset between the curves, stellar stripping would have to reduce the young stellar mass of an  $M_{\text{star,young}} = 10^{10} M_{\odot}$  galaxy by  $\sim 0.3$  dex to account for this offset. However, we will show in a forthcoming paper that stellar stripping within  $r_{200c}$  has a typical effect of  $< 0.1$  dex at these mass scales and can therefore not be a significant contributor to the lack of young stars within  $r_{200c}$ .

In contrast, galaxies with a given mass in old stars down to  $\sim 10^8 M_{\odot}$  are equally common within the virial radius as in the field (right-hand panel); this suggests that complete disruption of galaxies within  $r_{200c}$  is, likewise, not a significant contributor to the deficiency of low-mass galaxies in clusters. We therefore conclude that this is *predominantly due to the effect of star formation quenching*, which reduces the late-time growth of galaxies within  $r_{200c}$ . The quenching itself may have a variety of physical causes, including

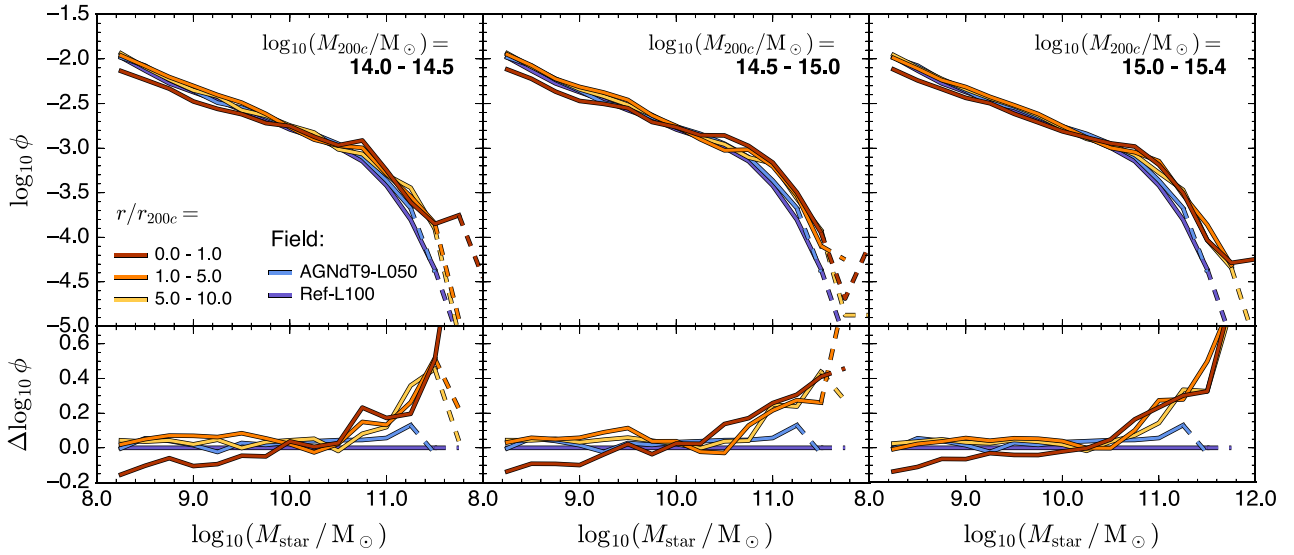


**Figure 7.** *Top row:* galaxy stellar mass function (GSMF) normalized to the total mass within the respective volume,  $\phi \equiv dn/d\log_{10}M_{\text{star}}/(M_{\text{tot}}/10^{10}M_{\odot})$ . Individual columns contain clusters of different  $M_{200c}$  (as indicated in the top right corner). Differently coloured lines (dashed where there are less than 10 galaxies per 0.25 dex bin) represent different radial zones in each cluster: inside  $r_{200c}$  (red); between 1 and 5  $r_{200c}$  (i.e. the region containing a population of backplash galaxies, orange); the far outskirts beyond 5  $r_{200c}$  (yellow). For comparison, the mass functions from the AGNdT9-L050 (blue) and Ref-L100 (purple) EAGLE runs are also shown. *Bottom row:* logarithmic ratio between each GSMF and that from the Ref-L100 periodic box. All halo mass bins show an excess of massive galaxies in and around clusters, without a clear radial trend. Galaxies less massive than  $\sim 10^{10}M_{\odot}$ , on the other hand, are deficient in the central cluster regions (red).

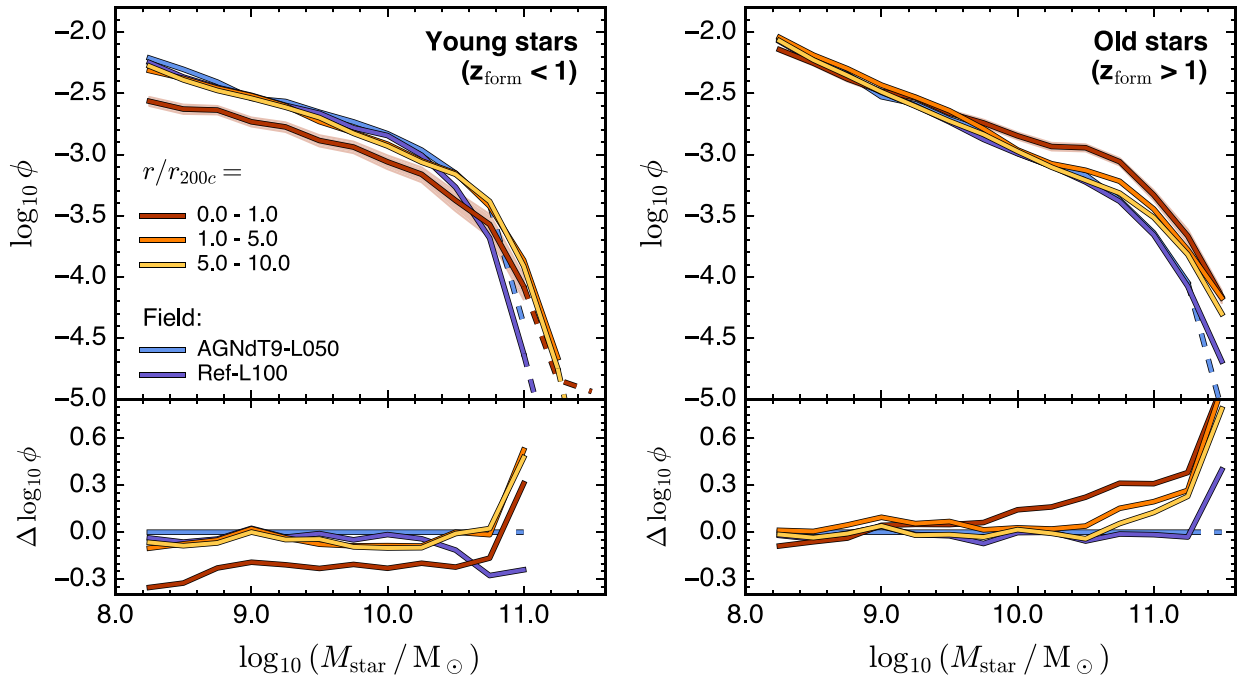


**Figure 8.** *Top panels:* the normalized  $z = 0$  galaxy stellar mass function (GSMF)  $\phi \equiv dn/d\log_{10}M_{\text{star}}/(M_{\text{tot}}/10^{10}M_{\odot})$  split by stellar formation redshift into ‘young’ stars ( $z_{\text{form}} < 1.0$ , left-hand panel) and ‘old’ stars ( $z_{\text{form}} > 1.0$ , right-hand panel). As in Fig. 7, the Hydrangea volumes are split into three radial zones (red, orange, and yellow lines) and compared to the EAGLE periodic-box simulations (blue/purple); dashed lines indicate bins with fewer than 10 galaxies. The shaded band, shown only for  $r < r_{200c}$  (red) for clarity, indicates the Poisson uncertainty on the GSMF. For clarity, the *bottom panels* show the logarithmic ratio between each GSMF and that from the AGNdT9-L050 periodic box. Evidently, the deficiency at low mass and excess of stellar mass at high mass are due to two different processes, since the former only affects young, and the latter mostly old stars.

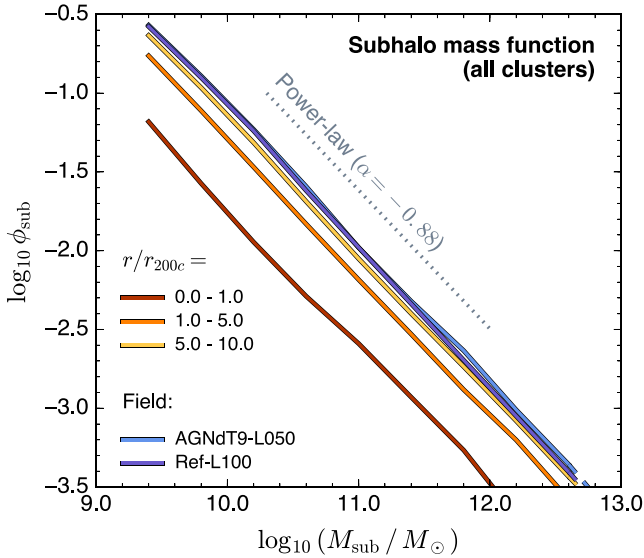


**Figure 9.** The normalized *subhalo* mass function (including central subhaloes) in and around the Hydrangea clusters, in analogy to the GSMF presented in Fig. 7. Masses are computed as the sum of all particles that are gravitationally bound to a given subhalo (including centrals). Different colours indicate different simulation zones and each mass function is normalized to the total mass in its respective zone. In contrast to the GSMF, all subhalo mass functions are near-perfect power laws with a slope of approximately  $-0.88$  (grey dotted line).

stripping of cold gas (Gunn & Gott 1972), unreplenished consumption of cold gas through star formation (e.g. Larson, Tinsley & Caldwell 1980; McGee, Bower & Balogh 2014), or stabilization of gas against collapse after the growth of a bulge (Martig et al. 2009). In future work, we will use the Hydrangea simulations to disentangle these mechanisms (see also Bahé & McCarthy 2015).

At the high-mass end, the right-hand panel of Fig. 8 demonstrates that the excess of galaxies is largely due to old stars. Their excess shows a systematic trend with radius, in the sense that galaxies with a high mass in old stars are most highly overabundant within  $r_{200c}$ , but a clear effect remains even at  $r > 5r_{200c}$  from the cluster centre. We will return to this in Section 4.2.2 below.

## 4.2 The galaxy–subhalo connection in and around clusters

### 4.2.1 Subhalo mass functions

An excess of massive galaxies in the vicinity of galaxy clusters may not be unexpected in  $\Lambda$ CDM, because the addition of large- and small-scale density peaks lead to earlier collapse of haloes, i.e. ‘assembly bias’ (e.g. Gao, Springel & White 2005; Gao & White 2007). We test the importance of this effect in Fig. 9, where we show the *subhalo* mass function, again comparing different zones in our cluster simulations and the periodic-box volumes from EAGLE, normalized by their total mass. Recall from above that our definition of ‘subhalo’ also includes the most massive bound structure within an FOF halo, i.e. the one hosting the central galaxy.

The subhalo mass functions differ markedly from the GSMF, and follow an almost perfect power law over 4 orders of magnitude in subhalo mass (from  $\sim 10^9$  to  $\sim 10^{13} M_\odot$ ). A power-law subhalo mass function agrees with previous cluster simulation studies, although there is a mild difference between the slopes. Our simulations yield a slope of  $\alpha \approx -0.88$  (see also Despali & Vegetti 2016 for the subhalo mass function in EAGLE), whereas Ghigna

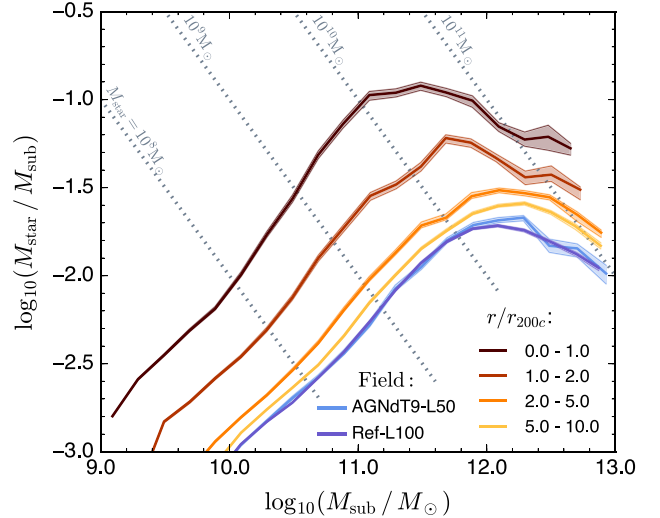


**Figure 10.** Median stellar mass fraction of Hydrangea  $z = 0$  subhaloes as a function of total subhalo mass  $M_{\text{sub}}$ , in different simulation zones (different colours). Shaded bands indicate  $1\sigma$  uncertainties on the median. Dashed lines are used where there are fewer than 10 galaxies per 0.2 dex bin. Grey dotted lines indicate the location of galaxies with constant stellar mass as indicated near the top. There is a striking shift of the distribution towards lower subhalo masses at approximately constant stellar mass near the cluster centre (darker lines), but also an offset towards higher stellar fractions on the far cluster outskirts.

et al. (2000) and Dolag et al. (2009) report a power-law slope of  $\alpha \approx -1$  in their  $N$ -body and lower-resolution hydrodynamical cluster simulations, respectively (the latter authors using the same subhalo finder as we do).<sup>12</sup>

The power-law slope is consistent between all three zones in our cluster simulations and the field, as determined from the original EAGLE simulations (blue/purple). The normalization, on the other hand, clearly depends on environment, with a suppression of  $\sim 0.7$  dex within  $r_{200c}$ , and a very small deficiency ( $\lesssim 0.1$  dex) even in the  $5-10 r_{200c}$  zone (orange). The former may partly reflect limitations in the SUBFIND subhalo finder (e.g. Muldrew et al. 2011), but these authors show that beyond  $\sim 1.5r_{200}$  SUBFIND does accurately recover the total masses of subhaloes, so this is unlikely to significantly affect the outermost zone. Irrespective of this, we can conclude that the excess of massive galaxies in and around clusters is not linked to an excess of (massive) subhaloes.

### 4.2.2 Stellar fractions of subhaloes

Our results above suggest that subhaloes (including centrals) in and around galaxy clusters have stellar mass fractions that differ from the field, which we confirm explicitly in Fig. 10. Field galaxies from the EAGLE simulations (blue/purple) show an increasing stellar fraction at low (sub-)halo mass, with a peak at subhalo masses of  $M_{\text{sub}} \approx 10^{12} M_\odot$  and subsequent decline towards higher masses; as Schaye et al. (2015) have shown, this behaviour agrees quantitatively with what is inferred from observations within the framework of abundance matching (e.g. Behroozi, Wechsler & Conroy 2013; Moster, Naab & White 2013).

<sup>12</sup> Ghigna et al. (2000) quote a power-law slope of  $-2$ , but this is for the mass function defined as  $dn/dM$ , not  $dn/d \log_{10} M$  as we show here.



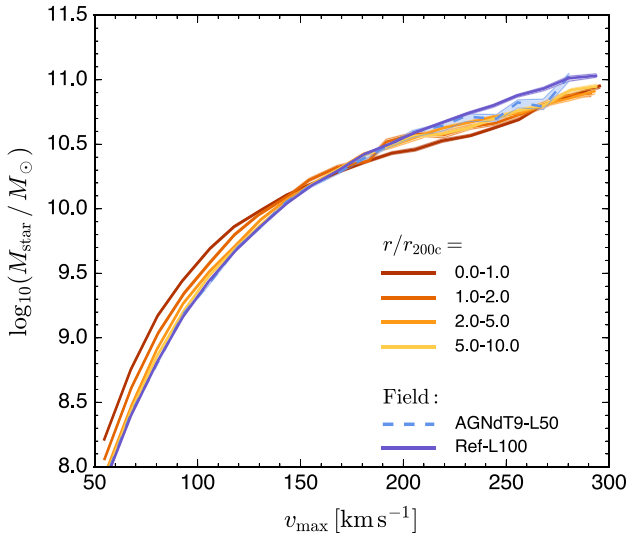


**Figure 11.** Stellar mass of Hydrangea galaxies as a function of maximum circular velocity,  $v_{\max}$ , compared to the field (blue/purple). In contrast to the comparison at fixed total mass presented in Fig. 10, there is no strong environmental offset for massive galaxies, with a small deficit of stellar mass in massive cluster galaxies compared to field galaxies of the same  $v_{\max}$ .

While cluster galaxies generally follow the same trend, there are two significant differences. At  $r < 2r_{200c}$ , stellar fractions are significantly higher at fixed  $M_{\text{sub}}$  than in the field, especially at low subhalo masses (e.g. a +1.4 dex offset at  $10^{11} M_{\odot}$  inside  $r_{200c}$ ), and the peak stellar fraction is shifted systematically to lower subhalo mass. Both of these differences are consistent with stripping of non-stellar mass (gas and DM), while the stellar mass remains constant, as indicated by the grey dotted lines in Fig. 10. To some extent, this may reflect artificial ‘stripping’ by the `SUBFIND` code, which may not detect all bound particles as members of the subhalo, but with Muldrew et al. (2011) reporting a detection efficiency of  $\sim 50$  per cent (0.3 dex) at  $0.5 r_{200c}$  (approximately the median radius of galaxies in the innermost bin), most of the stellar fraction difference is likely real. At least qualitatively, this agrees with the recent observational result of Niemiec et al. (2017), who report an increased stellar-to-halo mass for galaxies in the central regions of massive clusters compared to centrals. We note that they did not detect a significant enhancement beyond projected cluster-centric distances of 0.55 Mpc, in contrast to our findings here, but this is plausibly attributable to the relatively large uncertainties in their measurements.

At  $r > 2r_{200c}$ , stellar fractions remain higher than in the field, but the peak stellar fraction is located at approximately the same subhalo mass ( $M_{\text{sub}} \approx 10^{12} M_{\odot}$ ), or plausibly shifts slightly *higher* (by  $\lesssim 0.2$  dex). This excess can therefore not be explained by halo stripping, and instead suggests that *galaxy formation is more efficient near massive clusters*. A similar offset is seen when only considering central galaxies (not shown), so the offset is not due to differing fractions of satellites in different environments. We note that Moster et al. (2013) found a scatter of only  $\sim 0.15$  dex in the  $M_{\text{star}}-M_{\text{sub}}$  relation, which is much less than the systematic offset with environment identified here ( $\sim 0.3$  dex in the 2–5  $r_{200c}$  bin, and even stronger at smaller radii).

In contrast, Fig. 11 demonstrates that the stellar masses of galaxies at fixed maximum circular velocity ( $v_{\max}$ ), i.e. the Tully–Fisher relation (Tully & Fisher 1977), exhibit hardly any

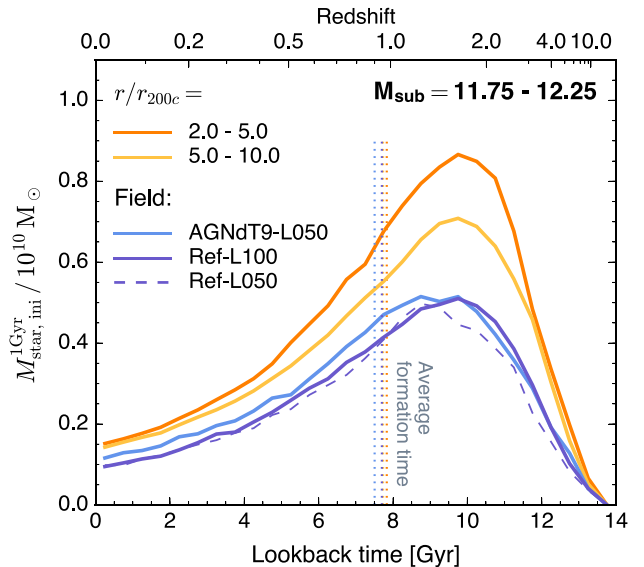


**Figure 12.** (Initial) stellar mass formed per Gyr as a function of lookback time in subhaloes of fixed total mass  $M_{\text{sub}} = 10^{11.75}-10^{12.25} M_{\odot}$  at  $z = 0$  in different environments. Blue/purple lines show field galaxies from EAGLE, while orange and yellow lines represent galaxies on the outskirts of Hydrangea clusters. The latter have had higher star formation throughout cosmic history, especially around  $z = 2$ . Vertical dotted lines show the corresponding mean formation redshifts, which are similar for all regions ( $z_{\text{av}} \approx 1$ ).

environmental variation in the Hydrangea simulations, at least at the massive end ( $v_{\max} \gtrsim 150 \text{ km s}^{-1}$ ). Furthermore, what little offset there is points in the opposite direction, i.e. galaxies around clusters contain marginally *less* stellar mass than in the field at fixed  $v_{\max}$ . This confirms previous findings that  $v_{\max}$  is a better predictor of stellar mass than (sub-)halo mass (e.g. Conroy, Wechsler & Kravtsov 2006; Reddick et al. 2013; Chaves-Montero et al. 2016).

### 4.3 Star formation histories

To probe the predicted differences between star formation in clusters and the field in more detail, we have reconstructed the star formation history of our galaxies by separating their star particles into 27 narrow bins of formation lookback time (0–13.5 Gyr, i.e.  $\Delta t = 500$  Myr) and summing up the initial stellar mass in each bin.<sup>13</sup> The result is shown in Fig. 12, where we compare the star formation histories of galaxies within subhaloes of similar total mass at redshift  $z = 0$  ( $M_{\text{sub}} \approx 10^{12} M_{\odot}$ ) in the two outer cluster zones (2–5 and 5–10  $r_{200c}$ ) of the Hydrangea simulations and in the EAGLE periodic boxes (as ‘field’). Star formation has been more efficient near clusters than in the field throughout cosmic history, but particularly around the cosmic SFR peak at  $z \approx 2$  (an excess of 67 per cent in the 2–5  $r_{200}$  zone compared to the field). We note that this does *not* necessarily imply that star formation was more efficient at equal  $z = 2$  subhalo mass, since (sub-)haloes near clusters are expected to have formed earlier (Gao et al. 2005) and will therefore have been more massive around the peak of star formation than subhaloes with the same  $z = 0$  mass in the field.

<sup>13</sup> Note that this is not necessarily identical to the SFR history of the main progenitor, since our approach also includes stars accreted through mergers.

As exemplified in the bottom row of Fig. 1, the high-redshift progenitors of our clusters typically consist of a collection of similarly massive protocluster cores linked by dense filaments. It is therefore perhaps not too surprising that even those galaxies that did not collapse into the central cluster at  $z = 0$  still experienced a high-redshift evolution that differed significantly from average regions of the Universe. These differences leave detectable imprints in the properties of galaxies on the far outskirts of clusters, which are less subject to late-time processes such as star formation quenching. We will investigate the mechanisms impacting galaxies in high-redshift protocluster regions in detail in future work.

#### 4.4 Halo concentrations

We have so far characterized subhaloes mainly by their total mass. However, for a galaxy like the Milky Way, the virial radius is  $\sim 300$  kpc, while star formation is restricted to the central  $\sim 10$  kpc. This opens the possibility that differences in the stellar-to-total mass ratio are caused by differences in halo concentrations: the more concentrated a halo is, the larger the fraction of its total mass (and plausibly also of its baryon content) that is compressed into the dense centre and can be turned into stars. In addition, the potential wells in more concentrated haloes are deeper so that feedback is less efficient, and because halo concentration correlates with formation time, such haloes will also have had more time to form stars. Matthee et al. (2017) have shown that, in EAGLE, at fixed halo mass galaxy stellar masses do indeed exhibit a positive correlation with the concentration of their host halo.

To test the hypothesis that this is the cause of the environmental trends we have identified above, we have computed the concentrations of FoF haloes in the Hydrangea simulations, as well as in EAGLE, in the same way as described in Section 2.2.3. To distinguish between stellar mass differences as cause and as effect of varying concentrations, we have done this for both the hydrodynamic simulations and the corresponding DMO runs, which are linked as described in Section 2.2.3. We did not compute concentrations for satellite subhaloes, because they do not have a well-defined virial radius, and hence focus here on central galaxies only.

We then compute a ‘field-equivalent’ concentration for each FoF halo in the hydrodynamic and DMO Hydrangea simulations. For this, we select all haloes in the EAGLE Ref-L100 and DMO-L100 simulation, respectively, whose  $\log_{10} M_{200c}$  differs by  $< 0.1$  from the Hydrangea halo under consideration. However, due to the steepness of the halo mass function, this sample of comparison EAGLE haloes will typically be biased towards the low-mass end of the  $M_{200c}$  selection range, and hence have a median concentration that is higher than that of the Hydrangea halo even in the absence of any real environmental differences. To mitigate this, we bin the EAGLE haloes into 10 narrow bins of  $\Delta \log_{10} M_{200c} = 0.02$  dex, and compute a median concentration weighted by the inverse number of haloes in each of these bins. Averaged over all Hydrangea haloes with  $M_{200c} > 10^{11} M_{\odot}$ , this weighting scheme results in a bias in  $M_{200c}$  that is less than 0.01 dex.

Fig. 13 shows the resulting concentration difference,  $\Delta c/c \equiv (c_{\text{Hydrangea}} - c_{\text{EAGLE}})/c_{\text{EAGLE}}$  as a function of  $r/r_{200c}$  for both the hydrodynamic (green) and DMO Hydrangea simulations (black), for haloes with  $M_{200c} > 10^{11.5} M_{\odot}$ . In both cases, solid lines indicate running medians while shaded bands represent  $1\sigma$  uncertainties. To compare the same haloes in both the DMO and hydrodynamic simulations, we selected them based on  $M_{200c}$  in the former, and then identified their counterparts in the latter via the links between their central subhaloes (see Section 2.2.3).

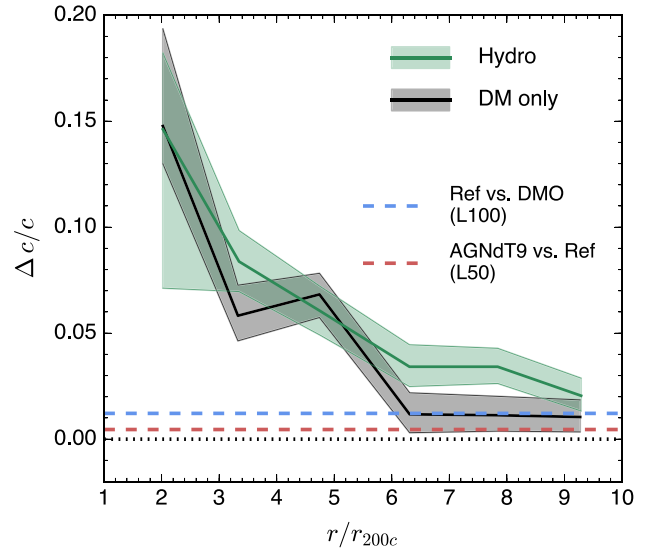


**Figure 13.** Relative difference in concentration of  $M_{200c} \geq 10^{11.5} M_{\odot}$  haloes on the outskirts of Hydrangea clusters compared to the field, as a function of distance from the central cluster (see the text for details). The green line compares hydrodynamic simulations, the black line the corresponding DMO runs. The two horizontal dashed lines indicate the difference in concentration between individually matched haloes in the EAGLE L100 Ref versus DMO simulations (blue) and L50 AGNdT9 versus Ref runs (red). An environmental enhancement of halo concentration persists to at least  $10 r_{200c}$ , is stronger in hydrodynamic than DMO simulations, and equals or exceeds concentration differences due to baryonic physics.

Halo concentrations are clearly affected by the proximity to a cluster. The effect is strongest for haloes closest to the cluster, with a median offset of 15 per cent at  $r \approx 2r_{200c}$ . This environmental effect is significantly greater than concentration differences arising from the presence of baryons in the field: this can be tested by linking haloes in the EAGLE Ref-L100 and DMO-L100 simulations in analogy to what we have done for Hydrangea, and only yields a concentration difference of  $\sim 1$  per cent in the halo mass range probed here (blue dashed line in Fig. 13). Even less significant are concentration differences arising from different parametrizations of AGN feedback, as we have tested by comparing the AGNdT9-L050 and Ref-L050 EAGLE simulations (red dashed line).

The environmental impact on halo concentrations decreases with increasing distance from the cluster, but does not reach zero even at the edge of our high-resolution region at  $\sim 10 r_{200c}$  (corresponding to distances of  $\sim 20$  Mpc). The difference between the hydrodynamic and DMO simulations is small, which rules out (potentially uncertain) baryon effects as its dominant cause.

A correlation between the concentration of DM haloes and their large-scale environment has already been demonstrated in DMO simulations (e.g. Wechsler et al. 2006; Gao & White 2007) and is also present in EAGLE (Chaves-Montero et al. 2016). These studies analysed the dependence between concentration and the clustering of haloes of similar mass, and found that, at the low-mass end, the most concentrated haloes are more clustered than the least concentrated ones, but that this effect reverses at  $M_{200c} \gtrsim 10^{13} M_{\odot}$ . Our results demonstrate that a concentration increase persists to haloes in the vicinity of massive clusters, even on their far outskirts.

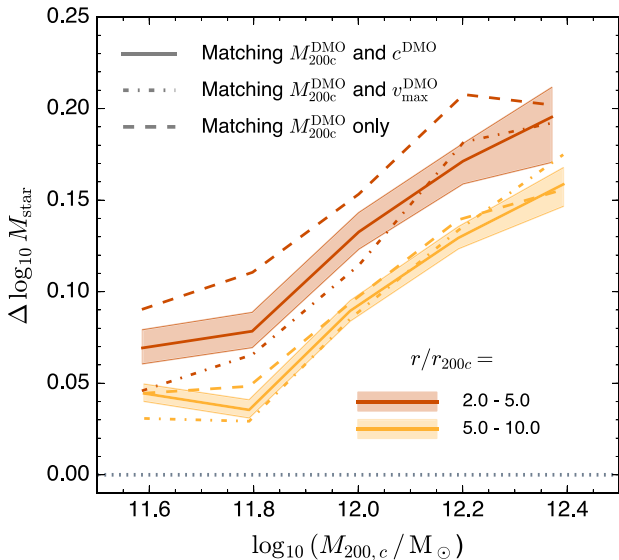


**Figure 14.** Excess stellar mass of central galaxies on the outskirts of clusters compared to the field. Galaxies are matched by the concentration and mass of their host halo (solid lines; shaded bands indicate statistical  $1\sigma$  uncertainties on the running median). For comparison, the excess from matching only by mass is shown with dashed lines, and that from matching by mass and maximum circular velocity as dash-dotted lines. The concentration difference (see Fig. 13) explains only a small part of the stellar mass excess around clusters, especially at  $r > 5r_{200c}$ .

#### 4.4.1 Connection between halo concentration and stellar mass

We have shown above that, at fixed halo mass, haloes near clusters contain more stellar mass and are more concentrated than in the field. We now test whether there is a connection between these two effects, by computing a ‘field-equivalent’ stellar mass from the EAGLE Ref-L100 simulation for each (central) Hydrangea galaxy, in analogy to the procedure for obtaining field-equivalent concentrations described above. As well as matching galaxies by  $M_{200c}$  only, we have also repeated the procedure with a simultaneous match in  $M_{200c}$  and  $c$ , requiring a maximum offset of 0.1 (0.05) in  $\log_{10} M_{200c}$  ( $\log_{10} c$ ) and computing weights as the product of the inverse number of galaxies in ten bins each in  $\log_{10} M_{200c}$  and  $\log_{10} c$ . Because the concentrations, as well as halo masses, in the hydrodynamic simulations might themselves be affected by baryonic processes associated with the higher stellar mass content, we compute both quantities in the corresponding DMO simulations and then link to the hydrodynamic runs as described in Section 2.2.3 for the stellar masses.

In Fig. 14, we show the difference between the actual and field-equivalent stellar mass of Hydrangea galaxies, i.e. the effect of environment at fixed halo mass and concentration. Perhaps surprisingly, galaxies in both radial zones still show a significant environmental mass excess, which reaches  $\sim 0.15$  dex at  $M_{\text{star}} \approx 10^{12.4} M_{\odot}$ . In fact, the excess is only marginally smaller than what is obtained without the additional match in concentration (dashed lines). The same is true when we match by the concentration as measured in the hydrodynamical, rather than DMO, simulation (not shown).

Evidently, higher halo concentrations are *not* the cause of the stellar mass excess around clusters, and instead the two effects result from different physical processes associated with a galaxy’s environment. Similarly, matching galaxies by  $v_{\text{max,DMO}}$  instead of  $c_{\text{DMO}}$  as second parameter (with a maximum offset of  $\Delta \log_{10} v_{\text{max}} = 0.05$ ) achieves no significant reduction in the stellar mass offset

(dash-dotted lines in Fig. 14). As we have shown in Fig. 11, the correlation between stellar mass and  $v_{\text{max}}$  as measured directly in the hydrodynamic simulations is largely insensitive to environment. The fact that the same does not apply to  $v_{\text{max,DMO}}$  indicates that the stellar mass offset near clusters is, in fact, not the result of differences between the DM haloes in the field and near clusters at fixed total mass, at least not to the extent that they are reflected in either their concentration or maximum circular velocity.<sup>14</sup> Rather, the enhanced stellar mass and maximum circular velocity (including baryons) appear to be *both* affected by an environmental effect that is predominantly, if not solely, due to baryons.

Our results from Fig. 14 are qualitatively consistent with what was shown by Croton, Gao & White (2007) with semi-analytic models applied to the Millennium Simulation (Springel et al. 2005b): these authors found that the excess clustering signal for red galaxies is only marginally reduced when concentration is used in addition to halo mass to shuffle galaxies in their simulated catalogues. In principle, it is possible that the embedding into the ICM halo and its surrounding filaments exerts pressure on galaxies near clusters and thus prevents feedback-driven outflows from escaping. However, this effect is not captured by semi-analytic models, and furthermore Bahé et al. (2012) showed that pressure confinement of satellite galaxies is generally ineffective. A more likely explanation is therefore that differences in the growth history of the (sub-)haloes hosting field and cluster galaxies lead to stronger imprints in the present-day stellar mass fraction than in their halo concentrations.

## 5 SUMMARY AND DISCUSSION

We have introduced the Hydrangea simulation suite, a set of 24 high-resolution cosmological hydrodynamical zoom-in simulations of massive galaxy clusters ( $M_{200c} = 10^{14.0} - 10^{15.4} M_{\odot}$ ) and their surroundings out to  $10 r_{200c}$  that form the key part of the C-EAGLE project. The simulations are run with the AGNdt9 galaxy formation model of the EAGLE suite (Schaye et al. 2015), and therefore allow a direct comparison between galaxy populations in the central regions of clusters, in their periphery, and in the field. They assume a *Planck* cosmology (Planck Collaboration XVI 2014b) and include subgrid prescriptions for radiative cooling, reionization, star formation, metal enrichment, and energy feedback from both star formation and accreting supermassive black holes (see Section 2.1). In this first paper, we have tested the stellar masses and star formation rates (SFRs) of our simulated galaxies, with the following main results:

(i) Our simulations broadly reproduce the observed total stellar mass fraction in galaxy clusters and predict a slightly sublinear scaling of stellar to halo mass. However, the stellar masses of simulated BCGs are too high by at least 0.2, and plausibly  $>0.5$ , dex. The total and BCG stellar masses of clusters on the outskirts of an even more massive cluster follow the same relation as isolated clusters (Fig. 4).

(ii) At  $z \approx 0$ , our simulations match several published satellite galaxy stellar mass functions (GSMFs). The only mild discrepancy concerns low-mass galaxies ( $M_{\text{star}} < 10^{10} M_{\odot}$ ), which are predicted

<sup>14</sup> As a direct test, we have also computed the stellar mass offsets equivalent to those shown in Fig. 14, but matching galaxies by the corresponding quantities derived from the hydrodynamical simulations (not shown). As expected from Fig. 11, this significantly reduces the offset when matching by  $M_{200c}$  and  $v_{\text{max}}$ , but leads to very similar results when matching by  $M_{200c}$  and  $c$  or  $M_{200c}$  alone.



to be somewhat less numerous than in the SDSS analysis of Yang et al. (2009, Fig. 5).

(iii) In qualitative agreement with observations, simulated cluster satellite galaxies have a quenched fraction ( $s\text{SFR} \equiv \text{SFR}/M_{\text{star}} < 10^{-11} \text{ yr}^{-1}$ ) that is higher than for centrals with the same stellar mass. The quenched fraction excess at  $M_{\text{star}} \gtrsim 10^{10} M_{\odot}$  is close to the observed value ( $\sim 60$  per cent at  $\sim 10^{10} M_{\odot}$ ). However, there are also quantitative discrepancies. The predicted quenched fractions of satellites decrease, rather than increase, with stellar mass. Furthermore, the quenched fractions of both centrals and satellites are lower than observed at  $M_{\text{star}} \gtrsim 10^{10} M_{\odot}$ , reaching only  $\sim 70$  per cent at  $M_{\text{star}} \approx 10^{11} M_{\odot}$  instead of near unity. At  $M_{\text{star}} \lesssim 10^{10} M_{\odot}$ , the quenched fraction of satellites is too high and shows an artificial increase towards lower stellar masses. This problem is not unique to our simulations, and plausibly results from insufficient resolution and an oversimplified modelling of the ISM (Fig. 6).

(iv) Normalized to total mass, the GSMF in our cluster simulations shows two subtle but significant differences from the field: a deficiency of low-mass ( $M_{\text{star}} \lesssim 10^{10} M_{\odot}$ ) galaxies within  $r_{200c}$ , and an excess of massive galaxies ( $M_{\text{star}} \gtrsim 10^{10} M_{\odot}$ ) from the centre to the far outskirts ( $\sim 10 r_{200c}$ ). Neither of these effects depends significantly on cluster mass (Fig. 7).

(v) The deficiency of low-mass galaxies within  $r_{200c}$  is not primarily caused by tidal stripping, but emerges as a consequence of star formation quenching: it is only present in young stars (formed at  $z < 1$ ), while the abundance of old stars in low-mass galaxies is consistent between clusters and the field (Fig. 8).

(vi) The excess of massive galaxies is not caused by an excess of massive subhaloes on the outskirts of our simulated clusters (Fig. 9), and instead originates from a significantly higher ( $\gtrsim 0.2$  dex) stellar fraction at a given subhalo mass (Fig. 10). This is found to be due to higher levels of star formation in (proto-)cluster environments than in the field, especially at redshift  $z \gtrsim 1$ , with an excess star formation of up to 67 per cent in subhaloes with  $M_{\text{sub}} \approx 10^{12} M_{\odot}$  compared to subhaloes with the same mass at  $z = 0$  in the field (Fig. 12).

(vii) At fixed mass, haloes near a cluster are more concentrated than in the field, out to  $\sim 10 r_{200c}$  from the cluster centre (Fig. 13). However, this does not explain the higher stellar mass fractions around clusters, because a similarly high stellar mass excess still remains between haloes of similar mass and concentration (Fig. 14).

The analysis presented here adds to the growing body of evidence that galaxy formation even far away from the centres of massive haloes is affected by the environment (e.g. Wetzel et al. 2012; Lu et al. 2012; Bahé et al. 2013). So far, large-scale environmental influence has been studied mainly in the context of the gas content and SFR of galaxies. According to our simulations, environment also affects the stellar masses of galaxies out to large radii, which is important because stellar mass is commonly used as the label to compare ‘similar’ galaxies in the field and in dense environments. This may lead to unexpected complications in the interpretation of observational results if relevant physical processes, such as ram pressure stripping, do not only depend significantly on stellar mass, but also on e.g. the halo mass. A comparison of galaxies in different environments matched only by  $M_{\text{star}}$  may then be fundamentally biased. In future work, we will explore the consequences of this bias in more detail.

It is also important to keep in mind that our simulation model was not calibrated in any way to produce realistic environmental effects on galaxies. As discussed by Schaye et al. (2015) and Crain et al. (2015), calibration of the EAGLE model primarily involved

the stellar masses and sizes of the overall galaxy population (i.e. mostly centrals), while the modifications to the AGN subgrid model in AGNdT9 compared to Ref were motivated by hot gas fractions in groups that were higher than observed. In light of this, the prediction of a quenched fraction excess, stellar mass function, and total stellar mass in massive clusters that are broadly consistent with observations is encouraging. Moreover, we demonstrate in a companion paper (Barnes et al. 2017b) that the hot gaseous haloes of our simulated clusters show approximately realistic global properties, such as hot gas fractions and X-ray emission, albeit with discrepancies in detail. The resolution of these, as well as improving the predicted quenched fractions of satellites as a function of stellar mass, will likely require further refinements to the modelling of feedback from AGN and star formation, as well as to the description of the dense, star-forming ISM.

In the future, we will exploit this potential of the Hydrangea simulations to understand how the formation of galaxies in and around massive clusters differs from that of isolated galaxies, in terms of e.g. their gas accretion, star formation activity, and morphological evolution.

## ACKNOWLEDGEMENTS

We thank the anonymous referee for a constructive report that improved the presentation of this paper. We also thank Lydia Heck for expert computational support with the Cosma machine in Durham, which was used for part of the work presented here. RAC is a Royal Society University Research Fellow. DJB and STK acknowledge support from Science & Technology Facilities Council (STFC) through grant ST/L000768/1. CDV acknowledges financial support from the Spanish Ministry of Economy and Competitiveness (MINECO) under the 2011 and 2015 Severo Ochoa Programmes SEV-2011-0187 and SEV-2015-0548, and grants AYA2014-58308 and RYC-2015-18078. PAT (ORCID 0000-0001-6888-6483) acknowledges support from the Science and Technology Facilities Council (grant no. ST/L000652/1). The Hydrangea simulations were in part performed on the German federal maximum performance computer ‘HazelHen’ at the maximum performance computing centre Stuttgart (HLRS), under project GCS-HYDA / ID 44067 financed through the large-scale project ‘Hydrangea’ of the Gauss Center for Supercomputing. Further simulations were performed at the Max Planck Computing and Data Facility (MPCDF) in Garching, Germany. This work also used the DiRAC Data Centric system at Durham University, operated by the Institute for Computational Cosmology on behalf of the STFC DiRAC HPC Facility ([www.dirac.ac.uk](http://www.dirac.ac.uk)). This equipment was funded by BIS National E-infrastructure capital grant ST/K00042X/1, STFC capital grant ST/H008519/1, and STFC DiRAC Operations grant ST/K003267/1 and Durham University. DiRAC is part of the National E-Infrastructure. We also gratefully acknowledge PRACE for awarding the EAGLE project access to the Curie facility based in France at Très Grand Centre de Calcul. Support was also received via the Interuniversity Attraction Poles Programme initiated by the Belgian Science Policy Office ([AP P7/08 CHARM]), the National Science Foundation under grant no. NSF PHY11-25915, and the UK Science and Technology Facilities Council (grant nos. ST/F001166/1 and ST/I000976/1) via rolling and consolidated grants awarded to the ICC. The research was supported by the Netherlands Organisation for Scientific Research (NWO), through VICI grant 639.043.409, and by the European Research Council under the European Union’s Seventh Framework Programme (FP7/2007-2013)/ERC grant agreement 278594-GasAroundGalaxies. This research has made use of NASA’s

Astrophysics Data System. All figures in this paper were produced using the `ASTROPY` (Astropy Collaboration et al. 2013) and `MATPLOTLIB` (Hunter 2007) PYTHON packages.

## REFERENCES

- Agertz O. et al., 2007, *MNRAS*, 380, 963
- Agulli I., Aguerri J. A. L., Sánchez-Janssen R., Barrena R., Diaferio A., Serra A. L., Méndez-Abreu J., 2014, *MNRAS*, 444, L34
- Agulli I., Aguerri J. A. L., Sánchez-Janssen R., Dalla Vecchia C., Diaferio A., Barrena R., Domínguez Palmero L., Yu H., 2016, *MNRAS*, 458, 1590
- Andreon S., 2010, *MNRAS*, 407, 263
- Astropy Collaboration et al., 2013, *A&A*, 558, A33
- Bahé Y. M., McCarthy I. G., 2015, *MNRAS*, 447, 969
- Bahé Y. M., McCarthy I. G., Crain R. A., Theuns T., 2012, *MNRAS*, 424, 1179
- Bahé Y. M., McCarthy I. G., Balogh M. L., Font A. S., 2013, *MNRAS*, 430, 3017
- Bahé Y. M. et al., 2016, *MNRAS*, 456, 1115
- Bahé Y. M., Schaye J., Crain R. A., McCarthy I. G., Bower R. G., Theuns T., McGee S. L., Trayford J. W., 2017, *MNRAS*, 464, 508
- Balogh M. L., Morris S. L., Yee H. K. C., Carlberg R. G., Ellingson E., 1999, *ApJ*, 527, 54
- Balogh M. L., Pearce F. R., Bower R. G., Kay S. T., 2001, *MNRAS*, 326, 1228
- Barnes D. J., Kay S. T., Henson M. A., McCarthy I. G., Schaye J., Jenkins A., 2017a, *MNRAS*, 465, 213
- Barnes D. J. et al., 2017b, *MNRAS*, preprint ([arXiv:1703.10907](https://arxiv.org/abs/1703.10907))
- Behroozi P. S., Wechsler R. H., Conroy C., 2013, *ApJ*, 770, 57
- Bell E. F., de Jong R. S., 2001, *ApJ*, 550, 212
- Bellstedt S. et al., 2016, *MNRAS*, 460, 2862
- Bocquet S., Saro A., Dolag K., Mohr J. J., 2016, *MNRAS*, 456, 2361
- Booth C. M., Schaye J., 2009, *MNRAS*, 398, 53
- Borgani S., Governato F., Wadsley J., Menci N., Tozzi P., Quinn T., Stadel J., Lake G., 2002, *MNRAS*, 336, 409
- Bower R. G., Schaye J., Frenk C. S., Theuns T., Schaller M., Crain R. A., McAlpine S., 2017, *MNRAS*, 465, 32
- Budzynski J. M., Kopusov S. E., McCarthy I. G., Belokurov V., 2014, *MNRAS*, 437, 1362
- Calvi R., Poggianti B. M., Vulcani B., Fasano G., 2013, *MNRAS*, 432, 3141
- Cameron E., 2011, *Publ. Astron. Soc. Aust.*, 28, 128
- Camps P., Trayford J. W., Baes M., Theuns T., Schaller M., Schaye J., 2016, *MNRAS*, 462, 1057
- Chabrier G., 2003, *PASP*, 115, 763
- Chang Y.-Y., van der Wel A., da Cunha E., Rix H.-W., 2015, *ApJS*, 219, 8
- Chaves-Montero J., Angulo R. E., Schaye J., Schaller M., Crain R. A., Furlong M., Theuns T., 2016, *MNRAS*, 460, 3100
- Conroy C., Wechsler R. H., Kravtsov A. V., 2006, *ApJ*, 647, 201
- Crain R. A. et al., 2009, *MNRAS*, 399, 1773
- Crain R. A. et al., 2015, *MNRAS*, 450, 1937
- Crain R. A. et al., 2017, *MNRAS*, 464, 4204
- Croton D. J., Gao L., White S. D. M., 2007, *MNRAS*, 374, 1303
- Cullen L., Dehnen W., 2010, *MNRAS*, 408, 669
- Dalla Vecchia C., Schaye J., 2012, *MNRAS*, 426, 140
- Despali G., Vegetti S., 2016, *MNRAS*, 469, 1997
- Dolag K., Borgani S., Murante G., Springel V., 2009, *MNRAS*, 399, 497
- Donahue M. et al., 2015, *ApJ*, 805, 177
- Dressler A., 1980, *ApJ*, 236, 351
- Dubois Y. et al., 2014, *MNRAS*, 444, 1453
- Durier F., Dalla Vecchia C., 2012, *MNRAS*, 419, 465
- Dutton A. A., Macciò A. V., 2014, *MNRAS*, 441, 3359
- Etherington J. et al., 2017, *MNRAS*, 466, 228
- Fabello S., Kauffmann G., Catinella B., Li C., Giovanelli R., Haynes M. P., 2012, *MNRAS*, 427, 2841
- Fabjan D., Borgani S., Tornatore L., Saro A., Murante G., Dolag K., 2010, *MNRAS*, 401, 1670
- Fasano G. et al., 2006, *A&A*, 445, 805
- Fogarty K., Postman M., Connor T., Donahue M., Moustakas J., 2015, *ApJ*, 813, 117
- Furlong M. et al., 2015, *MNRAS*, 450, 4486
- Furlong M. et al., 2017, *MNRAS*, 465, 722
- Gallazzi A., Charlot S., Brinchmann J., White S. D. M., Tremonti C. A., 2005, *MNRAS*, 362, 41
- Gao L., White S. D. M., 2007, *MNRAS*, 377, L5
- Gao L., Springel V., White S. D. M., 2005, *MNRAS*, 363, L66
- Gaspari M., Brighenti F., Ruszkowski M., 2013, *Astron. Nachr.*, 334, 394
- Geha M., Blanton M. R., Yan R., Tinker J. L., 2012, *ApJ*, 757, 85
- Ghigna S., Moore B., Governato F., Lake G., Quinn T., Stadel J., 2000, *ApJ*, 544, 616
- Giovanelli R., Haynes M. P., 1985, *ApJ*, 292, 404
- Gonzalez A. H., Zabludoff A. I., Zaritsky D., 2005, *ApJ*, 618, 195
- Gonzalez A. H., Sivanandam S., Zabludoff A. I., Zaritsky D., 2013, *ApJ*, 778, 14
- Gunn J. E., Gott J. R. III, 1972, *ApJ*, 176, 1
- Guo Q., White S., Angulo R. E., Henriques B., Lemson G., Boylan-Kolchin M., Thomas P., Short C., 2013, *MNRAS*, 428, 1351
- Haardt F., Madau P., 2001, in Neumann D. M., Tran J. T. V., eds, *Clusters of Galaxies and the High Redshift Universe Observed in X-rays*. CEA, Saclay, p. 64
- Hahn O., Martizzi D., Wu H.-Y., Evrard A. E., Teyssier R., Wechsler R. H., 2017, *MNRAS*, 470, 166
- Haines C. P. et al., 2009, *ApJ*, 704, 126
- Hansen S. M., Sheldon E. S., Wechsler R. H., Koester B. P., 2009, *ApJ*, 699, 1333
- Henriques B. M. B., White S. D. M., Thomas P. A., Angulo R. E., Guo Q., Lemson G., Springel V., 2013, *MNRAS*, 431, 3373
- Hess K. M., Wilcots E. M., 2013, *AJ*, 146, 124
- Hoffer A. S., Donahue M., Hicks A., Barthelmy R. S., 2012, *ApJS*, 199, 23
- Hopkins P. F., 2013, *MNRAS*, 428, 2840
- Hunter J. D., 2007, *Comput. Sci. Eng.*, 9, 90
- Jenkins A., 2010, *MNRAS*, 403, 1859
- Jenkins A., 2013, *MNRAS*, 434, 2094
- Katz N., White S. D. M., 1993, *ApJ*, 412, 455
- Kauffmann G. et al., 2003a, *MNRAS*, 341, 33
- Kauffmann G. et al., 2003b, *MNRAS*, 341, 54
- Kauffmann G., White S. D. M., Heckman T. M., Ménard B., Brinchmann J., Charlot S., Tremonti C., Brinkmann J., 2004, *MNRAS*, 353, 713
- Kennicutt R. C. Jr, 1998, *ApJ*, 498, 541
- Kravtsov A., Vikhlinin A., Meshcheryakov A., 2014, *Astrophys. J.*, preprint ([arXiv:1401.7329](https://arxiv.org/abs/1401.7329))
- Kron R. G., 1980, *ApJS*, 43, 305
- Lagos C. d. P. et al., 2015, *MNRAS*, 452, 3815
- Lan T.-W., Ménard B., Mo H., 2016, *MNRAS*, 459, 3998
- Larson R. B., Tinsley B. M., Caldwell C. N., 1980, *ApJ*, 237, 692
- Le Brun A. M. C., McCarthy I. G., Schaye J., Ponman T. J., 2014, *MNRAS*, 441, 1270
- Lidman C. et al., 2012, *MNRAS*, 427, 550
- Lu T., Gilbank D. G., McGee S. L., Balogh M. L., Gallagher S., 2012, *MNRAS*, 420, 126
- Marasco A., Crain R. A., Schaye J., Bahé Y. M., van der Hulst T., Theuns T., Bower R. G., 2016, *MNRAS*, 461, 2630
- Martig M., Bournaud F., Teyssier R., Dekel A., 2009, *ApJ*, 707, 250
- Martizzi D., Jimmy Teyssier R., Moore B., 2014, *MNRAS*, 443, 1500
- Matthee J., Schaye J., Crain R. A., Schaller M., Bower R., Theuns T., 2017, *MNRAS*, 465, 2381
- McAlpine S., Bower R. G., Harrison C. M., Crain R. A., Schaller M., Schaye J., Theuns T., 2017, *MNRAS*, 468, 3395
- McCarthy I. G. et al., 2010, *MNRAS*, 406, 822
- McCarthy I. G., Schaye J., Bower R. G., Ponman T. J., Booth C. M., Dalla Vecchia C., Springel V., 2011, *MNRAS*, 412, 1965
- McCarthy I. G., Schaye J., Bird S., Le Brun A. M. C., 2017, *MNRAS*, 465, 2936
- McGee S. L., Bower R. G., Balogh M. L., 2014, *MNRAS*, 442, L105

- Mitchell N. L., McCarthy I. G., Bower R. G., Theuns T., Crain R. A., 2009, *MNRAS*, 395, 180
- Moster B. P., Naab T., White S. D. M., 2013, *MNRAS*, 428, 3121
- Muldrew S. I., Pearce F. R., Power C., 2011, *MNRAS*, 410, 2617
- Neto A. F. et al., 2007, *MNRAS*, 381, 1450
- Niemiec A. et al., 2017, preprint ([arXiv:1703.03348](https://arxiv.org/abs/1703.03348))
- Peng Y.-j. et al., 2010, *ApJ*, 721, 193
- Planck Collaboration I, 2014a, *A&A*, 571, A1
- Planck Collaboration XVI, 2014b, *A&A*, 571, A16
- Popesso P., Biviano A., Böhringer H., Romaniello M., 2006, *A&A*, 445, 29
- Price D. J., 2008, *J. Comput. Phys.*, 227, 10040
- Qu Y. et al., 2017, *MNRAS*, 464, 1659
- Ragone-Figueroa C., Granato G. L., Murante G., Borgani S., Cui W., 2013, *MNRAS*, 436, 1750
- Rahmati A., Schaye J., Pawlik A. H., Raicevic M., 2013, *MNRAS*, 431, 2261
- Rahmati A., Schaye J., Bower R. G., Crain R. A., Furlong M., Schaller M., Theuns T., 2015, *MNRAS*, 452, 2034
- Rasmussen J., Mulchaey J. S., Bai L., Ponman T. J., Raychaudhury S., Dariush A., 2012, *ApJ*, 757, 122
- Reddick R. M., Wechsler R. H., Tinker J. L., Behroozi P. S., 2013, *ApJ*, 771, 30
- Rosas-Guevara Y. M. et al., 2015, *MNRAS*, 454, 1038
- Rosas-Guevara Y., Bower R. G., Schaye J., McAlpine S., Dalla Vecchia C., Frenk C. S., Schaller M., Theuns T., 2016, *MNRAS*, 462, 190
- Sánchez S. F. et al., 2013, *A&A*, 554, A58
- Scannapieco C. et al., 2012, *MNRAS*, 423, 1726
- Schaller M. et al., 2015a, *MNRAS*, 451, 1247
- Schaller M. et al., 2015b, *MNRAS*, 452, 343
- Schaller M., Dalla Vecchia C., Schaye J., Bower R. G., Theuns T., Crain R. A., Furlong M., McCarthy I. G., 2015c, *MNRAS*, 454, 2277
- Schaye J., 2004, *ApJ*, 609, 667
- Schaye J., Dalla Vecchia C., 2008, *MNRAS*, 383, 1210
- Schaye J., Theuns T., Rauch M., Efstathiou G., Sargent W. L. W., 2000, *MNRAS*, 318, 817
- Schaye J. et al., 2010, *MNRAS*, 402, 1536
- Schaye J. et al., 2015, *MNRAS*, 446, 521
- Sijacki D., Springel V., Di Matteo T., Hernquist L., 2007, *MNRAS*, 380, 877
- Springel V., 2005, *MNRAS*, 364, 1105
- Springel V., White S. D. M., Tormen G., Kauffmann G., 2001, *MNRAS*, 328, 726
- Springel V., Di Matteo T., Hernquist L., 2005a, *MNRAS*, 361, 776
- Springel V. et al., 2005b, *Nature*, 435, 629
- Stott J. P. et al., 2010, *ApJ*, 718, 23
- Theuns T., Schaye J., Zaroubi S., Kim T.-S., Tzanavaris P., Carswell B., 2002a, *ApJ*, 567, L103
- Theuns T., Bernardi M., Frieman J., Hewett P., Schaye J., Sheth R. K., Subbarao M., 2002b, *ApJ*, 574, L111
- Tormen G., Bouchet F. R., White S. D. M., 1997, *MNRAS*, 286, 865
- Trayford J. W. et al., 2015, *MNRAS*, 452, 2879
- Trayford J. W. et al., 2017, *MNRAS*, 470, 771
- Tremonti C. A. et al., 2004, *ApJ*, 613, 898
- Tully R. B., Fisher J. R., 1977, *A&A*, 54, 661
- Velliscig M., van Daalen M. P., Schaye J., McCarthy I. G., Cacciato M., Le Brun A. M. C., Dalla Vecchia C., 2014, *MNRAS*, 442, 2641
- Vikhlinin A. et al., 2009, *ApJ*, 692, 1033
- Vogelsberger M. et al., 2014, *MNRAS*, 444, 1518
- von der Linden A., Wild V., Kauffmann G., White S. D. M., Weinmann S., 2010, *MNRAS*, 404, 1231
- Vulcani B. et al., 2011, *MNRAS*, 412, 246
- Vulcani B., De Lucia G., Poggianti B. M., Bundy K., More S., Calvi R., 2014, *ApJ*, 788, 57
- Wang W., White S. D. M., 2012, *MNRAS*, 424, 2574
- Wechsler R. H., Zentner A. R., Bullock J. S., Kravtsov A. V., Allgood B., 2006, *ApJ*, 652, 71
- Weinmann S. M., van den Bosch F. C., Yang X., Mo H. J., Croton D. J., Moore B., 2006, *MNRAS*, 372, 1161
- Wendland H., 1995, *Adv. Comput. Math.*, 4, 389
- Wetzel A. R., Tinker J. L., Conroy C., 2012, *MNRAS*, 424, 232
- White S. D. M., Rees M. J., 1978, *MNRAS*, 183, 341
- Wiersma R. P. C., Schaye J., Smith B. D., 2009a, *MNRAS*, 393, 99
- Wiersma R. P. C., Schaye J., Theuns T., Dalla Vecchia C., Tornatore L., 2009b, *MNRAS*, 399, 574
- Yang X., Mo H. J., van den Bosch F. C., Pasquali A., Li C., Barden M., 2007, *ApJ*, 671, 153
- Yang X., Mo H. J., van den Bosch F. C., 2009, *ApJ*, 695, 900

## APPENDIX A: SUMMARY OF HYDRANGEA CLUSTERS

In Table A1, we provide information about each of the 30 C-EAGLE clusters at  $z = 0$ . Masses are computed as the total mass within spherical apertures centred on the potential minimum of the cluster within which the average density equals 200 (500) times the critical, as well as 200 times the mean, density of the Universe. Concentrations are obtained as described in Section 2.2.3, by fitting an NFW profile to the DM density profile between 0.05 and  $1 r_{200c}$ , following Neto et al. (2007) and Schaller et al. (2015b). The position coordinates  $x$ ,  $y$ , and  $z$  (in units of pMpc) specify the centre of each re-simulation region in the original parent simulation (see Barnes et al. 2017b and Appendix B for a description of how our high-resolution ICs were generated). The dominance measure ( $D_5$ ) specifies the distance (in pMpc) from the central cluster to the nearest halo with  $M_{200c}$  at least 1/5 of the central cluster.  $D_5$  is calculated from the parent DMO simulation, because not all zoom regions contain such a massive secondary halo within their high-resolution region. Finally, we give the number of galaxies with  $M_{\text{star}} \geq 10^9 M_{\odot}$  within 1 and  $10 r_{200c}$  ( $5 r_{200c}$  for the six simulations that are not part of Hydrangea) from the potential minimum of the central cluster.



**Table A1.** Overview of the 30 C-EAGLE simulations at redshift  $z = 0$ . The 24 Hydrangea simulations with high-resolution regions extending to at least  $10 r_{200c}$  from the cluster centre are listed first. The last six entries, below the horizontal line, represent the six additional haloes simulated only out to  $5 r_{200c}$ . We provide the radii within which the average density equals 200 (500) times the critical, and 200 times the mean, density; the total mass enclosed in these radii, as well as the stellar mass within  $r_{500c}$ ; the centre of the zoom-in region in the  $(3200 \text{ pMpc})^3$  parent simulation; the best-fitting NFW concentration of the central cluster halo; the dominance parameter  $D_5$ , defined as the distance to the nearest halo whose mass is at least one fifth of that of the central cluster (determined from the parent simulation); and the number of galaxies with  $M_{\text{star}, 30\text{pkpc}} \geq 10^9 M_\odot$  within 1 and  $10 r_{200c}$  from the potential minimum of the cluster. X-ray properties of the central clusters at  $z = 0.1$  are provided in the companion paper by Barnes et al. (2017b). <sup>†</sup>For the six clusters simulated only to  $5r_{200c}$ , the last column instead gives the number of galaxies within this radius.

| Halo ID | $r_{200c}$ | $r_{200m}$<br>(pMpc) | $r_{500c}$ | $M_{200c}$ | $M_{200m}$<br>[ $\log_{10}(M/M_\odot)$ ] | $M_{500c}$ | $M_{500c}^{\text{star}}$ | $x$     | $y$<br>(pMpc) | $z$     | $c_{\text{NFW}}$ | $D_5$<br>(pMpc) | $N_{\text{galaxies}} < r_{200c}$ | $< 10r_{200c}$    |
|---------|------------|----------------------|------------|------------|--|------------|--------------------------|---------|---------------|---------|------------------|-----------------|----------------------------------|-------------------|
| CE-0    | 1.03       | 1.74                 | 0.68       | 14.07      | 14.24                                    | 13.92      | 12.21                    | 313.65  | 2218.64       | 2652.71 | 5.3              | 11.4            | 36                               | 181               |
| CE-1    | 1.02       | 1.63                 | 0.65       | 14.05      | 14.15                                    | 13.87      | 12.16                    | 2598.97 | 2552.80       | 2266.29 | 3.7              | 6.9             | 34                               | 163               |
| CE-2    | 1.02       | 1.63                 | 0.65       | 14.05      | 14.15                                    | 13.87      | 12.16                    | 2889.69 | 2880.09       | 355.44  | 6.1              | 15.8            | 34                               | 163               |
| CE-3    | 1.09       | 1.84                 | 0.70       | 14.14      | 14.31                                    | 13.97      | 12.15                    | 2608.58 | 2831.41       | 908.38  | 6.5              | 9.9             | 49                               | 243               |
| CE-4    | 1.17       | 1.89                 | 0.78       | 14.23      | 14.34                                    | 14.10      | 12.29                    | 1720.84 | 2253.49       | 2670.52 | 4.2              | 5.2             | 68                               | 322               |
| CE-5    | 1.09       | 1.90                 | 0.72       | 14.15      | 14.35                                    | 13.99      | 12.29                    | 583.22  | 908.50        | 1669.79 | 6.7              | 14.2            | 42                               | 294               |
| CE-6    | 1.27       | 2.16                 | 0.81       | 14.34      | 14.52                                    | 14.15      | 12.35                    | 2624.03 | 2241.14       | 304.69  | 3.6              | 17.6            | 76                               | 380               |
| CE-7    | 1.27       | 2.17                 | 0.81       | 14.34      | 14.53                                    | 14.16      | 12.37                    | 1272.32 | 2452.95       | 1288.05 | 4.6              | 7.5             | 76                               | 452               |
| CE-8    | 1.23       | 2.12                 | 0.79       | 14.30      | 14.49                                    | 14.12      | 12.36                    | 486.08  | 735.81        | 357.66  | 4.5              | 16.2            | 67                               | 338               |
| CE-9    | 1.39       | 2.36                 | 0.92       | 14.46      | 14.63                                    | 14.32      | 12.48                    | 1368.63 | 1452.69       | 2207.20 | 5.2              | 9.1             | 84                               | 486               |
| CE-10   | 1.29       | 2.21                 | 0.82       | 14.36      | 14.55                                    | 14.17      | 12.45                    | 2616.89 | 1602.52       | 1876.43 | 4.8              | 10.3            | 90                               | 446               |
| CE-11   | 1.43       | 2.34                 | 0.94       | 14.49      | 14.63                                    | 14.35      | 12.51                    | 2564.49 | 678.34        | 1356.74 | 6.5              | 8.8             | 109                              | 537               |
| CE-12   | 1.55       | 2.49                 | 1.03       | 14.60      | 14.71                                    | 14.47      | 12.71                    | 1165.85 | 1386.20       | 1010.20 | 4.7              | 26.5            | 148                              | 506               |
| CE-13   | 1.57       | 2.52                 | 1.07       | 14.61      | 14.72                                    | 14.51      | 12.63                    | 998.80  | 1511.46       | 1963.65 | 6.3              | 11.4            | 131                              | 498               |
| CE-14   | 1.62       | 2.66                 | 0.98       | 14.66      | 14.79                                    | 14.41      | 12.52                    | 276.94  | 1459.94       | 2042.48 | 2.5              | 10.8            | 179                              | 734               |
| CE-15   | 1.71       | 2.73                 | 1.05       | 14.73      | 14.83                                    | 14.49      | 12.74                    | 2015.45 | 737.45        | 1738.86 | 2.2              | 6.4             | 203                              | 957               |
| CE-16   | 1.74       | 2.84                 | 1.17       | 14.75      | 14.88                                    | 14.63      | 12.76                    | 717.52  | 2244.68       | 609.33  | 7.0              | 9.2             | 202                              | 1179              |
| CE-18   | 1.87       | 3.03                 | 1.23       | 14.84      | 14.96                                    | 14.70      | 12.64                    | 793.71  | 864.02        | 1612.59 | 4.8              | 27.0            | 261                              | 1061              |
| CE-21   | 1.99       | 3.34                 | 1.24       | 14.93      | 15.09                                    | 14.71      | 12.87                    | 1139.47 | 909.91        | 948.80  | 3.3              | 11.9            | 306                              | 1901              |
| CE-22   | 2.14       | 3.72                 | 1.39       | 15.02      | 15.23                                    | 14.86      | 12.85                    | 2078.36 | 2319.21       | 843.85  | 4.4              | 5.2             | 362                              | 3153              |
| CE-24   | 2.27       | 3.61                 | 1.52       | 15.09      | 15.19                                    | 14.97      | 12.82                    | 306.88  | 996.23        | 2870.46 | 5.0              | 21.9            | 425                              | 1701              |
| CE-25   | 2.36       | 3.87                 | 1.47       | 15.15      | 15.28                                    | 14.93      | 12.91                    | 1028.05 | 1272.37       | 1276.27 | 2.5              | 20.6            | 497                              | 2185              |
| CE-28   | 2.50       | 4.06                 | 1.68       | 15.22      | 15.34                                    | 15.10      | 13.02                    | 1390.16 | 1049.82       | 2040.15 | 3.7              | 16.2            | 556                              | 2804              |
| CE-29   | 2.82       | 4.61                 | 1.61       | 15.38      | 15.51                                    | 15.04      | 12.96                    | 1070.13 | 2140.38       | 1498.16 | 1.8              | 30.1            | 826                              | 3788              |
| CE-17   | 1.65       | 2.74                 | 1.02       | 14.68      | 14.83                                    | 14.45      | 13.07                    | 216.56  | 1847.43       | 2889.33 | 2.7              | 14.5            | 180                              | 381 <sup>†</sup>  |
| CE-19   | 1.86       | 3.07                 | 1.21       | 14.84      | 14.98                                    | 14.68      | 13.13                    | 805.68  | 319.03        | 1136.84 | 3.4              | 9.0             | 291                              | 704 <sup>†</sup>  |
| CE-20   | 1.77       | 2.87                 | 1.16       | 14.78      | 14.89                                    | 14.62      | 13.15                    | 2693.84 | 1783.70       | 2955.12 | 5.0              | 14.4            | 216                              | 449 <sup>†</sup>  |
| CE-23   | 1.99       | 3.34                 | 1.31       | 14.92      | 15.09                                    | 14.77      | 12.92                    | 2033.86 | 2989.23       | 2715.06 | 3.1              | 10.0            | 314                              | 848 <sup>†</sup>  |
| CE-26   | 2.39       | 3.89                 | 1.56       | 15.16      | 15.29                                    | 15.00      | 13.23                    | 2818.50 | 1262.96       | 1993.58 | 5.5              | 11.6            | 468                              | 1083 <sup>†</sup> |
| CE-27   | 2.39       | 3.82                 | 1.64       | 15.16      | 15.26                                    | 15.07      | 13.16                    | 2646.97 | 913.51        | 2629.65 | 7.2              | 20.2            | 252                              | 475 <sup>†</sup>  |

## APPENDIX B: GENERATION OF INITIAL CONDITIONS

Based on the 3.2 cGpc parent simulation (Barnes et al. 2017a), zoomed ICs for our cluster re-simulations were generated with the second-order Lagrangian perturbation theory code `IC_2LPT_GEN` (Jenkins 2010) and using the public `PANPHASIA` white noise field (Jenkins 2013).<sup>15</sup> This approach is similar to what was done by Barnes et al. (2017a) for the MACSIS project and is described in more detail in the companion paper by Barnes et al. (2017b). As described in Section 2.2.2, we required that a sphere of radius  $10 r_{200c}$  around each cluster centre – defined as the potential minimum of the cluster halo – be free from low-resolution boundary particles at redshift  $z = 0$ . Within this high-resolution region, particle masses are nearly the same<sup>16</sup> as in the ‘intermediate’ resolution

runs of the EAGLE suite, i.e.  $m_{\text{DMO}} \approx 1.15 \times 10^7 M_\odot$ . From these DMO ICs, the ICs including baryons were derived as described in appendix B2 of Schaye et al. (2015): each original particle is split into one DM and one SPH (gas) particle, with a mass ratio of  $\Omega_{\text{baryon}}/(\Omega_{\text{matter}} - \Omega_{\text{baryon}}) = 0.186$ . The initial baryon particle mass in our hydrodynamic simulations is therefore  $m_{\text{baryon}} \approx 1.81 \times 10^6 M_\odot$  and the DM particle mass is  $m_{\text{DM}} \approx 9.7 \times 10^6 M_\odot$ .

As a technical detail, we note that the particle indexing in C-EAGLE (including Hydrangea) is different from EAGLE. In the latter, the particle IDs in the original DMO ICs encode the particle’s position along the Peano–Hilbert curve (see appendix B3 of Schaye et al. 2015). While this makes it easy to link each particle to its initial position, it leads to very large ID numbers that cannot easily be used as keys to compare particles between different outputs. In C-EAGLE (including Hydrangea), the original DMO IDs are therefore assigned in running order from 1 to  $N_{\text{part}}$ . As in EAGLE,

<sup>15</sup> The phase descriptor of the parent simulation is [Panph1, L14, (2152, 5744, 757), S3, CH1814785143, EAGLE\_L3200\_VOL1].

<sup>16</sup> The particle masses realized by our zoom-in ICs generator cannot be specified to arbitrary precision, as they are formed from  $10^3$  glass tiles that have

to be accommodated within the masked region. The actual particle masses therefore vary slightly between different zoom simulations, by  $< 3$  per cent.

when we create the full hydrodynamic ICs, the ID of the DM particle is assigned to be exactly twice that of the original particle, and that of the gas particle one more than its corresponding DM particle; thus all DM particles have even, and all baryon particles odd, ID numbers.

### APPENDIX C: TRACING OF SUBHALOES BETWEEN OUTPUTS

To fully utilize the information provided by our simulations, it is necessary to be able to link galaxies between outputs to reconstruct their individual formation histories. Although the results presented in this paper do not rely significantly on this ability, we will exploit this information in future work. For reference, we therefore describe here our subhalo tracing method, which is adapted from Bahé & McCarthy (2015). We will in this context use the term ‘galaxy’ to refer to the physical entity that is present in multiple snapshots (irrespective of whether its stellar mass is zero or not), and the term ‘subhalo’ for each individual identification of a galaxy in one snapshot.

Our tracing procedure exploits the ability to identify individual DM particles in different snapshots through their unique particle IDs. As a first step, we link in each pair of neighbouring snapshots any two subhaloes that share at least 20 DM particles, as long as these particles represent at least one per cent of all DM particles in the lower redshift snapshot. We note that in Bahé & McCarthy (2015), we had also included star particles to allow tracing galaxies beyond the point of disruption of their DM halo. This is not done here, because the improved resolution of the Hydrangea simulations means that even subhaloes with a DM mass of only  $\sim 2 \times 10^8 M_\odot$  are resolved by 20 DM particles.

In the simplest possible scenario, each subhalo in a given snapshot  $i$  would ‘receive’ only one link from a subhalo in the preceding snapshot ( $i - 1$ ), and ‘send’ one link to a subhalo in the subsequent snapshot ( $i + 1$ ). In this case, we could unambiguously identify these subhaloes as representing the same galaxy in all three snapshots.

In reality, however, galaxies are expected to exchange particles between each other (e.g. in mergers), so that one subhalo identified in snapshot  $i$  will, in general, be linked to multiple others in  $i + 1$  (and vice versa). As a second step, we therefore have to select the best-matching links between  $i$  and  $i + 1$ . For this purpose, we rank all links sent from a given subhalo in  $i$ , and all those received by a given subhalo in  $i + 1$ , by their total mass – i.e. the sum of the particle masses contributing to this link, which in our DMO case is equivalent to the number of particles. In this way, each link is assigned a ‘sender rank’ and a ‘receiver rank’. We then select those links with the highest receiver rank at each subhalo in  $i + 1$ . If one subhalo in  $i$  sends multiple links with equal receiver ranks, only the one with the highest sender rank is considered out of these.

In practice, the majority of selected links are those with the highest receiver rank, i.e. those contributing the largest amount of DM particles to a given subhalo in snapshot  $i + 1$ . Under certain circumstances, it may however be appropriate to select a link with a lower receiver rank, in particular if multiple links received and sent by one subhalo have comparable masses (e.g. in complex mergers). After selecting the receiver-rank 0 links, we therefore then iterate through the nine next-highest receiver ranks at each subhalo which have a mass of at least two-thirds of the highest rank link (if they exist), and select from those in analogy with the rank-0 selection described above.

The reason for this double ranking (by sender and receiver) is that it prevents situations where a small subhalo accreted on to a

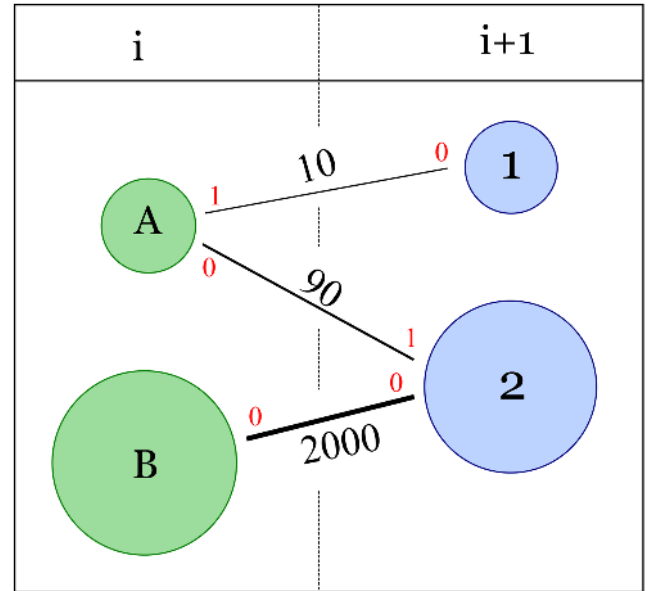


**Figure C1.** Schematic example of the links between four subhaloes in two consecutive snapshots. As explained in the text, our tracing algorithm ensures that subhaloes A and 1 are linked into one galaxy, rather than being treated as merged on to 2.

more massive one is misidentified as the latter’s progenitor, while allowing subhaloes that lose the majority of their mass due to, for example tidal stripping, to be traced for as long as possible. We repeat this process for each pair of neighbouring snapshots to obtain a continuous history of all galaxies in our simulation. In each snapshot, any subhalo that has no receiving link selected is assumed to represent a newly formed galaxy.

As an illustration of this linking procedure, consider the situation depicted in Fig. C1: two subhaloes each in consecutive snapshots ( $i$ ,  $i + 1$ ) are connected by three links with 10, 90, and 2000 particles, respectively. It is unambiguous that subhaloes B and 2 represent the same galaxy, since they are each other’s best-matching progenitor and descendant. Subhalo A, on the other hand, could be treated as either having merged with 2, or as representing the same galaxy as 1, but with most of its matter transferred on to subhalo 2 (e.g. through tidal stripping). We prefer the second option, since it maximizes the time for which a galaxy orbiting in a cluster can be tracked.

An additional complication is that subhalo finders such as SUBFIND are known to have difficulty identifying subhaloes in dense backgrounds, such as the central regions of a galaxy cluster (e.g. Muldrew et al. 2011). Unaccounted for, this would lead to spurious subhalo ‘disruption’ (when a subhalo still physically exists, but is not identified as such) and ‘formation’ (if it is re-identified later). To mitigate this, we also trace subhaloes over two consecutive snapshot intervals by forming what we call ‘long links’ between each pair of snapshots separated by one snapshot between them, in analogy to the ‘short links’ described above. In the simplest case, the temporary non-identification will leave a subhalo A in the first snapshot  $i$  without a (short-link) descendant, and a counterpart B in the second snapshot ( $k \equiv i + 2$ ) without a (short-link) progenitor. Provided A and B are connected by a long link, we can then join them together from  $i$  to  $k$  and skip the missing identification in snapshot  $j$  in-between.

However, it is also possible that between redshifts  $i$  and  $k$ , the subhalo accretes another, smaller subhalo, which would then be identified as its progenitor although physically it is not (cf. above).

We therefore also allow selection of long links between subhaloes that already have an identified (short-link) progenitor or descendant in the immediately neighbouring snapshot, provided this results in a better match of particles between subhaloes.

The procedure described above allows our code to robustly follow self-bound structures through time, accounting for subhalo formation, merging and disruption, as well as temporary

non-identification of subhaloes in dense environments. In the future, we also intend to run alternative substructure identification and subhalo tracing codes on our galaxy cluster simulations, and to compare the results.

This paper has been typeset from a  $\text{\TeX}/\text{\LaTeX}$  file prepared by the author.